



Solar Cycle Variability Induced by Tilt Angle Scatter in a Babcock–Leighton Solar Dynamo Model

Bidya Binay Karak and Mark Miesch

High Altitude Observatory, National Center for Atmospheric Research, 3080 Center Green Dr., Boulder, CO 80301, USA; bkarak@ucar.edu

Received 2017 March 8; revised 2017 July 28; accepted 2017 August 11; published 2017 September 21

Abstract

We present results from a three-dimensional Babcock–Leighton (BL) dynamo model that is sustained by the emergence and dispersal of bipolar magnetic regions (BMRs). On average, each BMR has a systematic tilt given by Joy’s law. Randomness and nonlinearity in the BMR emergence of our model produce variable magnetic cycles. However, when we allow for a random scatter in the tilt angle to mimic the observed departures from Joy’s law, we find more variability in the magnetic cycles. We find that the observed standard deviation in Joy’s law of $\sigma_\delta = 15^\circ$ produces a variability comparable to the observed solar cycle variability of $\sim 32\%$, as quantified by the sunspot number maxima between 1755 and 2008. We also find that tilt angle scatter can promote grand minima and grand maxima. The time spent in grand minima for $\sigma_\delta = 15^\circ$ is somewhat less than that inferred for the Sun from cosmogenic isotopes (about 9% compared to 17%). However, when we double the tilt scatter to $\sigma_\delta = 30^\circ$, the simulation statistics are comparable to the Sun ($\sim 18\%$ of the time in grand minima and $\sim 10\%$ in grand maxima). Though the BL mechanism is the only source of poloidal field, we find that our simulations always maintain magnetic cycles even at large fluctuations in the tilt angle. We also demonstrate that tilt quenching is a viable and efficient mechanism for dynamo saturation; a suppression of the tilt by only 1° – 2° is sufficient to limit the dynamo growth. Thus, any potential observational signatures of tilt quenching in the Sun may be subtle.

Key words: dynamo – magnetohydrodynamics (MHD) Sun: magnetic fields – Sun: activity – (Sun:) sunspots – Sun: interior – Sun: rotation

1. Introduction

The 11-year solar cycle is a manifestation of the oscillatory magnetic field of the Sun. The solar cycle, however, is not regular. The strength and the period have an irregular variation. The extreme example of such variation is the Maunder minimum in the 17th century, when sunspots largely disappeared for about 70 years. Indirect studies suggest that there were many such events in the past (Usoskin 2013).

There is no doubt that a dynamo mechanism, operating in the solar convection zone (SCZ), is responsible for producing the solar magnetic cycle. Thus the natural way to study the solar dynamo is by solving the basic magnetohydrodynamic (MHD) equations in a rotating spherical shell, encompassing the SCZ. However, though substantial progress has been made in recent years in studying fundamental dynamo mechanisms (e.g., Charbonneau 2014; Augustson et al. 2015; Featherstone & Miesch 2015; Hotta et al. 2016; Käpylä et al. 2016; Karak & Brandenburg 2016), MHD simulations still cannot capture all processes relevant to the solar dynamo and the solar cycle (Fan & Fang 2014; Karak et al. 2015). One reason could be that these simulations do not produce sufficient flux emergence in the form of tilted bipolar magnetic regions (BMRs) that we see in the solar observations (e.g., Wang & Sheeley 1989). These tilted BMRs, when they decay and disperse on the solar surface, produce a large-scale poloidal field, as proposed by Babcock (1961) and Leighton (1964). Recent high-quality BMR (area, tilt, separation, and so on) and polar field data (measured both directly via polarization and indirectly through different proxies, including polar faculae and active networks) suggest that this process is sufficient to maintain the observed polar flux in the Sun (Dasi-Espuig et al. 2010; Kitchatinov & Olemskoy 2011; Muñoz-Jaramillo et al. 2013; Priyal et al. 2014).

In the Babcock–Leighton (BL) paradigm, the poloidal flux produced by the decay of tilted BMRs gets transported downward, to the bulk of the SCZ, by meridional circulation and convection. There the differential rotation stretches this poloidal field to produce a toroidal component—the Ω effect. This toroidal flux then produces BMRs on the surface consistent with the Hale polarity rule (Hale et al. 1919; Stenflo & Kosovichev 2012), although there are some difficulties in constraining how and where BMRs are formed. By comparing the observed magnetic flux on the solar surface with the flux generated by the differential rotation, Cameron and Schüssler (2015) have argued that the Ω effect can account for the toroidal flux that ultimately emerges as BMRs. This suggests that the solar dynamo is of the $\alpha_{\text{BL}}\Omega$ type, where α_{BL} is the symbol for the BL process. Following this basic dynamo loop and using the turbulent diffusivity and meridional flow for the flux transport, many authors have developed 2D as well as 3D BL dynamo models (see reviews by Charbonneau 2010; Karak et al. 2014a). Most of these models have been able to reproduce the basic features of the solar cycle.

Possible causes of solar cycle variability in the BL dynamo framework include variations in (1) convective transport, (2) the meridional circulation, (3) the differential rotation, and (4) the BL process. Note that Lorentz forces play a role in all of these mechanisms, so they are not listed as a separate item.

Flux transport by convective flows (1) definitely has stochastic elements and nonlinear feedbacks due to the dynamo-generated magnetic field and has been studied by some authors (e.g., Kitchatinov et al. 1994; Karak et al. 2014b). However, this is a challenging problem that will require a unified understanding of small- and large-scale dynamo action to fully address. The influence of the meridional circulation in particular (2) has been investigated by a number of authors and

has been shown to give rise to cycle variability, including grand minima and grand maxima (e.g., Charbonneau & Dikpati 2000; Lopes & Passos 2009; Karak & Choudhuri 2011, 2013; Upton & Hathaway 2014). Weak variations in the differential rotation (3) are known to exist, namely torsional oscillations. However, the observed correlation between the polar flux at cycle minimum and the sunspot number of the following cycle suggests that the Ω effect may be largely linear and therefore not a major source of cycle variability (Jiang et al. 2007; Wang & Sheeley 2009; Muñoz-Jaramillo et al. 2013).

Here we focus on mechanism (4), namely the variability induced by the BL process. The poloidal field generated in this process largely depends on the amount of flux in BMRs, the frequency of BMR eruptions, and the tilt angles of BMRs. All of these quantities have temporal variations. Since, on average, there are only about two new BMRs per day on the solar surface, the fluctuations in any of these quantities can lead to a considerable variation in the poloidal field and consequently the cycle strength.

In this work, we investigate mechanism (4) in an innovative way, using our 3D STABLE (Surface flux Transport And Babcock–Leighton) solar dynamo model (Miesch & Dikpati 2014; Miesch & Teweldebirhan 2016; hereafter MD14 and MT16, respectively). We focus in particular on the influence of the observed tilt angle distribution by superposing a random scatter on the Joy’s law prescription that we used in previous work. We have also introduced tilt angle quenching into STABLE as a mechanism for dynamo saturation.

In addition to implementing tilt angle scatter, we have also modified the flux distribution of BMRs. Previously, the flux of each BMR was directly linked to the low-latitude toroidal flux at the base of the CZ. In this study, we improve the realism of the model by choosing a BMR flux distribution based on solar observations. Furthermore, we consider two alternative ways to regulate the photospheric flux budget. The first is to increase the amount of magnetic flux in each BMR by shifting the flux distribution toward larger values when the toroidal flux near the base of the CZ is large. The second is to keep the flux distribution the same and vary the rate of BMR emergence in response to the toroidal flux near the base of the CZ. In this latter approach, the range of emergence rates we use is consistent with solar observations.

In our study, we first ask several questions, namely, whether the solar dynamo can be maintained through the observed properties of BMRs without any other source of the poloidal field, whether the quenching in the tilt angle is sufficient to saturate the dynamo, and how robust this model is with different algorithms of BMR deposition frequency and with different values of diffusivity. Then, we explore the variation of the magnetic cycle due to the observed variation in the BMR tilt angles.

Random scatter in BMR tilt angles has been proposed by many authors as a possible mechanism to explain the irregularity of the solar cycle, and it has been studied previously within the context of 2D BL dynamo models (e.g., Charbonneau & Dikpati 2000; Jiang et al. 2007; Choudhuri & Karak 2009; Olesnkoy & Kitchatinov 2013), surface flux transport (SFT) models (Jiang et al. 2014; Hathaway & Upton 2016), and in a coupled 2D \times 2D BL/SFT dynamo model (Lemerle & Charbonneau 2017). However, to our knowledge, our model is the first 3D solar dynamo model to explicitly investigate the

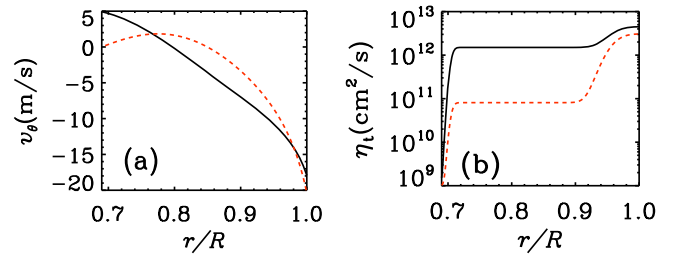


Figure 1. Radial variations of (a) the latitudinal component of the velocity v_θ at midlatitude and (b) the turbulent diffusivity η_t used in the advection-dominated model (dashed red line) and the diffusion-dominated model (solid line).

implications of tilt angle scatter with regard to solar cycle variability.

After analyzing the features of magnetic cycles obtained from this model, we explore whether the variation in the tilt angle can also lead to extreme cycle modulation, such as grand minima and maxima. Finally, we explore the robustness of our model and, in particular, whether it continues to produce magnetic cycles when the tilt angle scatter becomes very large.

2. Model

In our model, we solve the induction equation

$$\frac{\partial \mathbf{B}}{\partial t} = \nabla \times \{(\mathbf{V} + \gamma) \times \mathbf{B} - \eta_t \nabla \times \mathbf{B}\} \quad (1)$$

in three dimensions (r, θ, ϕ) for the whole SCZ with $0.69R \leq r \leq R$ (R = radius of the Sun), $0 \leq \theta$ (colatitude) $\leq \pi$, and $0 \leq \phi \leq 2\pi$. In the simulations reported here, our model is kinematic, and the velocity field \mathbf{V} is composed of axisymmetric meridional circulation (v_r and v_θ) and differential rotation ($v_\phi/r \sin \theta$), such that

$$\mathbf{V} = v_r(r, \theta) \hat{\mathbf{r}} + v_\theta(r, \theta) \hat{\boldsymbol{\theta}} + r \sin \theta \Omega(r, \theta) \hat{\boldsymbol{\phi}}. \quad (2)$$

For the meridional circulation, we use the profile given in many previous publications, particularly in Karak & Cameron (2016; Equation (5)), which closely resembles the surface observations. Hence, without repeating the mathematical equations of this flow, we just make a few comments: near the surface it is poleward with a maximum speed of 20 m s^{-1} , near the base of the CZ it is equatorward with a speed of about 2 m s^{-1} , and it smoothly goes to zero at the lower boundary ($0.69R$); see the dashed line in Figure 1(a).

Note that in this study we have considered a single cell circulation. Recent helioseismic inversions suggest that this may not be accurate, but they have not yet converged on a robust determination of what the structure and amplitude may in fact be (Jackiewicz et al. 2015; Rajaguru & Antia 2015; Zhao & Chen 2016). In the absence of this information and to make contact with previous BL dynamo models, we have retained the single-celled profile. Others have investigated the role of multicelled circulation profiles in 2D BL/flux transport dynamo models, and they have demonstrated that these models are still viable, provided that the circulation near the base of the convection zone is equatorward and that the convective transport of the poloidal flux (typically parameterized by a turbulent diffusion and a magnetic pumping) is sufficiently efficient (Jouve & Brun 2007; Hazra et al. 2014; Belucz et al. 2015; Hazra & Nandy 2016).

For differential rotation, we use an analytic function that captures the observed helioseismic data. This profile has been used in many previous publications; for example, see Equation (3) of MT16.

The γ , appearing as an advective term in Equation (1), is the magnetic pumping. In most of the simulations, we include a downward magnetic pumping, motivated by the study of Karak & Cameron (2016). Thus we write $\gamma = \gamma_r(r)\hat{r}$, where

$$\gamma_r(r) = -\frac{\gamma_{\text{CZ}}}{2} \left[1 + \operatorname{erf}\left(\frac{r - 0.725R}{0.01R}\right) \right] - \frac{\gamma_S}{2} \left[1 + \operatorname{erf}\left(\frac{r - 0.9R}{0.02R}\right) \right]. \quad (3)$$

Due to the lack of knowledge of the exact latitudinal variation of γ_r , we take it to be only a function of radius. As discussed in Karak & Cameron (2016), the pumping is efficient near the surface (mainly caused by the topological asymmetry of the convective flow), while the deeper convection is weaker and less stratified (Spruit 1997). The pumping helps to boost the efficiency of the dynamo by suppressing the diffusion of toroidal flux through the surface. The amount of pumping used in each simulation varies depending on the value of diffusivity used. Hence γ_{CZ} and γ_S will have different values in different simulations.

In the present model, we do not consider the small-scale convective flow, and thus to capture its mixing effect, we consider an effective turbulent diffusivity represented by η_t in Equation (1). This is actually the sum of the molecular and turbulent diffusivities. We do not have a reliable estimate of η_t in the deep CZ. The mixing-length theory and other theoretical studies suggest that the value of η_t in the midconvection zone is of the order of $10^{12} \text{ cm}^2 \text{ s}^{-1}$ (Parker 1979; Miesch et al. 2012; Cameron and Schüssler 2016; Simard et al. 2016). Near the surface, at least, it is fairly constrained by observations, as well as by the SFT model (e.g., Komm et al. 1995; Lemerle et al. 2015), and it is about a few times $10^{12} \text{ cm}^2 \text{ s}^{-1}$. Hence, in our model, we choose the following radial dependent profile for η_t :

$$\eta_t(r) = \eta_{\text{RZ}} + \frac{\eta_{\text{CZ}}}{2} \left[1 + \operatorname{erf}\left(\frac{r - 0.715R}{0.0125R}\right) \right] + \frac{\eta_S}{2} \left[1 + \operatorname{erf}\left(\frac{r - 0.956R}{0.025R}\right) \right], \quad (4)$$

where $\eta_{\text{RZ}} = 1.0 \times 10^9 \text{ cm}^2 \text{ s}^{-1}$, and $\eta_S = 3 \times 10^{12} \text{ cm}^2 \text{ s}^{-1}$. We have broadly two sets of simulations. In one set, $\eta_{\text{CZ}} = 5 \times 10^{10} \text{ cm}^2 \text{ s}^{-1}$, while in the other set, $\eta_{\text{CZ}} = 1.5 \times 10^{12} \text{ cm}^2 \text{ s}^{-1}$; see Figure 1(b). Thus the first set of simulations will be close to our previous publications (MD14, MT16) in terms of the diffusion, while the latter set will be in the so-called diffusion-dominated regime, where diffusive flux transport across the CZ dominates over advection by the meridional circulation (e.g., Jiang et al. 2007; Yeates et al. 2008).

A major component of our model is the SpotMaker algorithm, which deposits BMRs on the surface based on the toroidal flux near the base of the convection zone. In SpotMaker, we do the following steps. First, we compute the strength of the

spot-producing toroidal flux near the base of the CZ:

$$\hat{B}(\theta, \phi, t) = \int_{r_a}^{r_b} h(r) B_\phi(r, \theta, \phi, t) dr, \quad (5)$$

where $r_a = 0.715R$, $r_b = 0.73R$, and $h(r) = h_0(r - r_a)/(r_b - r)$ with h_0 as a normalization factor. We note that to have a prominent equatorward migration of sunspots, the spot-producing toroidal flux is computed above the tachocline where the flow is strongest. A necessary (but not sufficient) condition to produce a BMR is that $\hat{B}(\theta, \phi, t)$ exceeds a threshold field strength $B_t(\theta)$. If this condition is satisfied on multiple grid points, then out of those points, one point is chosen randomly. Unlike previous publications (MD14, MT16), where a fixed value was taken for this threshold field strength, here we make it dependent on latitude such that it increases exponentially toward the higher latitudes. Hence we choose

$$B_t(\theta) = B_{t0} \exp[\gamma(\theta - \pi/2)], \quad \text{for } \theta > \pi/2 \\ = B_{t0} \exp[\gamma(\pi/2 - \theta)], \quad \text{for } \theta \leq \pi/2, \quad (6)$$

where $\gamma = 5$ and $B_{t0} = 2 \text{ kG}$. The rapid increase of B_t in latitude is chosen to have sufficient spots near the equator and no spots beyond about $\pm 30^\circ$ latitudes. The advantage of using such latitude-dependent B_t is that now we do not have to choose any arbitrary masking function to suppress spots above a certain latitude, which was used in many previous works (e.g., Dikpati et al. 2004; MD14). Another advantage is that now the upper latitudinal bound for BMR emergence is not fixed, and it can vary depending on the toroidal field strength in each cycle and even in each hemisphere. This is consistent with observations that stronger cycles start producing sunspots at slightly higher latitudes (Solanki et al. 2008). Other than some tachocline instabilities that might be operating in higher latitudes to destabilize the spot-producing toroidal field (Gilman & Dikpati 2000; Parfrey & Menou 2007; Dikpati et al. 2009), we have to confess that, at the moment, we do not have a clear understanding of why BMRs do not appear above a certain latitude, and the arbitrary masking function or the latitude-dependent B_t chosen here may be regarded as a semiempirical model.

When SpotMaker produces a BMR, we do not reduce the flux locally at the progenitor location, although we do place opposing flux near the surface by virtue of the 3D structure of the BMRs; see Section 2.3 of MT16 for details on this issue. Therefore, at every time step of our numerical integration, if the BMR emergence is determined only by the criterion $\hat{B}(\theta, \phi) > B_t(\theta)$, then we may have BMRs emerging at every time step, and the total number of BMRs will largely be determined by the integration time step and the value of B_{t0} . Thus, to make the emergence rate independent of the numerics and more realistic, we specify a time delay between two successive BMRs based on solar observations. The time delay distribution obtained from the observed sunspot data (Royal Observatory Greenwich—USAF/NOAA sunspots¹) during 1900–2002 is shown by the thick solid line in Figure 2. We

¹ Compiled by David Hathaway, <http://solarscience.msfc.nasa.gov/greenwch.shtml>.

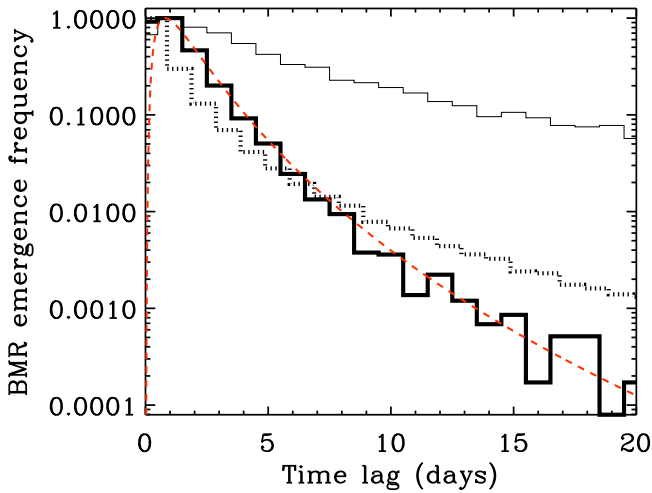


Figure 2. Normalized histograms of the time delays between the successive BMR emergences obtained from the observed data during 1900–2002. The thick solid line is obtained by taking data within a three-year window at each cycle maximum, while the thin solid line represents the rest of the data, covering the solar minimum periods. The dashed red line is the fitted log-normal distribution with $\{\tau_p, \tau_s\} \equiv \{0.8, 1.9\}$ days, as given by Equation (7). The dotted line is obtained from our model (Run B9), in which the time delay is related to the magnetic field through Equation (12) in Section 4.

approximate this data by a log-normal distribution given by

$$P(\Delta) = \frac{1}{\sigma_d \Delta \sqrt{2\pi}} \exp \left[-\frac{(\ln \Delta - \mu_d)^2}{2\sigma_d^2} \right], \quad (7)$$

where σ_d and μ_d are specified in terms of the mean τ_s and mode τ_p of the distribution such that $\sigma_d^2 = (2/3)[\ln \tau_s - \ln \tau_p]$ and $\mu_d = \sigma_d^2 + \ln \tau_p$. When $\tau_p = 0.8$ days and $\tau_s = 1.9$ days, the above log-normal distribution reasonably fits the observed data, as shown by the red dashed line in Figure 2. We, however, note that the observed time delay shown by the thick solid line in Figure 2 is obtained only from the three years of data during each solar maximum, and not from the full period of 1900–2002 data. Actually, during the solar minimum, we observe less frequent BMR, and the time delay is much longer; see the thin solid line in Figure 2. Thus the time delay, in reality, is cycle-phase dependent—it is shortest at the peak of the cycle and longest at the minimum. However, as a first step, we shall perform a set of simulations by taking fixed values of $\tau_p = 0.8$ days and $\tau_s = 1.9$ days, obtained from the solar maxima data. Later, in Section 4, we shall implement a solar-cycle-dependent time delay by considering τ_p and τ_s as dependent on the toroidal field. We note that the time delay in each hemisphere is always computed separately using Equation (7) so that no hemispheric symmetry is imposed in this process.

Just to summarize the whole idea, SpotMaker produces the first BMR once the condition $\hat{B}(\theta, \phi) > B_t(\theta)$ is satisfied. Then after a time dt since the time of the previous BMR appearance, the SpotMaker produces the next BMR only when both conditions $\hat{B}(\theta, \phi) > B_t(\theta)$ and $dt \geq \Delta^{N(S)}$, where $\Delta^{N(S)}$ is the time delay randomly obtained from the long-normal distribution given by Equation (7) for the northern (or southern) hemisphere. The superscript “ $N(S)$ ” on Δ is to emphasize that the time delay between BMRs can be different in two

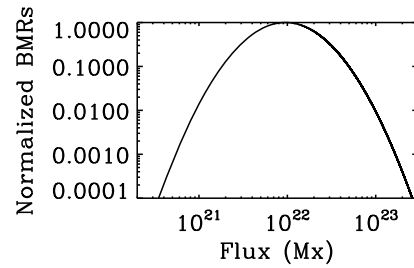


Figure 3. Normalized flux distribution of BMRs used in our dynamo model.

hemispheres because the probability is computed separately in two hemispheres.

Once SpotMaker decides to produce a BMR on the surface, we need to specify its flux, tilt, separation, and spatial distribution. In comparison to previous publications (MD14; MT16; Hazra et al. 2017), here we have some changes in order to make a close connection with observations. In the previous model, the BMR flux was directly related to the toroidal field at the base of the CZ, while in this model, it is obtained from the observed distribution. The observed BMR flux distribution can be approximated using a log-normal distribution:

$$P(\Phi) = \Phi_0 \frac{1}{\sigma_\Phi \Phi \sqrt{2\pi}} \exp \left[-\frac{(\ln \Phi - \mu_\Phi)^2}{2\sigma_\Phi^2} \right], \quad (8)$$

with $\mu_\Phi = 51.2$ and $\sigma_\Phi = 0.77$. Certainly, in the low-flux regime, a log normal is not the best fit of the observed flux as there are many BMRs with fluxes smaller than 5×10^{21} Mx. However, smaller BMRs may not contribute much net poloidal flux because of their smaller flux and large scattered tilts (Stenflo & Kosovichev 2012). The above distribution with $\Phi_0 = 1$, plotted in Figure 3, is obtained from Muñoz-Jaramillo et al. (2015) based on observations of *Solar and Heliospheric Observatory*/Michelson Doppler Imager magnetograms during 1996–2010. Different data sets in their publication produced slightly different values of μ_Φ and σ_Φ (see also Zhang et al. 2010; Lemerle et al. 2015). Once the flux of the BMR is obtained from the above distribution, the radius is automatically set by specifying a fixed value for the surface field strength of 3 kG. As discussed in MT16, if this radius turns out to be comparable to or smaller than the grid size of the domain, then we set the radius at five times the grid size, and the field strength is reduced accordingly.

The half distance between centers of two spots of a BMR is chosen to be 1.5 times the radius of the spot. As in our earlier model, we have assumed spots to be disconnected from their parent spot-producing fields. The surface fields are extrapolated downward using a potential field approximation as described in MT16, which yields the full 3D structure of a BMR. In our model, BMRs are assumed to be rather shallow by choosing the radial field of the spots to be zero at $r_s = 0.9R$.

In our previous publications (MD14; MT16), we have used the standard Joy’s law, $\delta = \delta_0 \cos \theta$ (Hale et al. 1919; Dasi-Espuig et al. 2010; Stenflo & Kosovichev 2012), for tilt angles of BMRs. Here we make two modifications in it. One is made by adding a random component δ_f around Joy’s law. In observations, we notice that Joy’s law is a statistical law, and there is a considerable scatter around it (Howard 1991; Stenflo & Kosovichev 2012; McClintock et al. 2014; Senthamizh

Pavai et al. 2015). Particularly, from the analysis of BMRs measured during 1976–2008, Wang et al. (2015) reported that the fluctuations of the tilts roughly follow a Gaussian distribution:

$$f(\delta_f) = \frac{1}{\sigma_\delta \sqrt{2\pi}} \exp[-\delta_f^2 / (2\sigma_\delta^2)], \quad (9)$$

with $\sigma_\delta \approx 15^\circ$. We understand that a Gaussian is not the best fit to the observed fluctuations of the data because of its asymmetric shape and considerable outliers near the two ends of the distribution. However, to capture the broad picture of the tilt fluctuations in our model, the above Gaussian distribution is sufficient (see also Figure 3 of Stenflo & Kosovichev 2012 for the distribution of BMR tilts within 15° – 20° latitudes). Another modification to Joy’s law that we implement here is the tilt angle saturation; the tilt is suppressed for strong progenitor toroidal fields. Thus the tilt used in our model is given by

$$\delta = \frac{\delta_0 \cos \theta + \delta_f}{1 + (\hat{B}(\theta, \phi, t) / B_{\text{sat}})^2}, \quad (10)$$

where $\delta_0 = 35^\circ$ and B_{sat} (the saturation field strength) is chosen to be 1×10^5 G. In thin flux tube simulations, tilts of the BMRs are produced by the Coriolis force acting on the toroidal flux tubes during their rise in the CZ (e.g., D’Silva & Choudhuri 1993; Fan et al. 1994). When the spot-producing toroidal field is strong, the field rises fast and the Coriolis force does not get much time to tilt it. Thus, from this theoretical argument, we expect some quenching in the tilt (see Işık 2015 for a possible explanation of tilt quenching along this line). In observations, we find some evidence of tilt quenching with the BMR flux (Dasi-Espuig et al. 2010; Stenflo & Kosovichev 2012), although the picture is less transparent because of the lack of detailed analysis. In any case, we shall explore whether the above magnetic-field-dependent nonlinearity is sufficient to stabilize the growth of the magnetic field in Equation (1), and in future work, we shall consider other possible saturation mechanisms. We note that in our previous model (MD14; MT16) dynamo saturation was implemented by saturating the flux content of BMRs rather than their tilt. The tilt angle saturation we use here has more physical justification.

For boundary conditions, we use a radial field on the surface and a perfect conductor at the lower boundary. For the initial seed field, we use a weak dipolar magnetic field.

3. Results for Fixed BMR Delay Distribution

As discussed in Sections 1 and 2, we consider two ways in which the photospheric flux is linked to the deep toroidal flux. The first is by making the BMR flux proportional to the deep toroidal flux. These runs are labeled with “A” and discussed in this section. The second is to fix the flux distribution and instead link the BMR emergence rate to the deep toroidal flux. These runs are described in Section 4.

For the model with fixed delay distribution, we scale the observed BMR flux with the toroidal field at the base of the CZ, such that the BMR flux in the model is $\Phi_s = (\hat{B}(\theta_s, \phi_s, t) / B_{\text{sat}}) \Phi$. Here, (θ_s, ϕ_s) is the location of the BMR, and Φ is the BMR flux obtained from the observed distribution given in Equation (8). Using this BMR flux and other ingredients as specified in Section 2, we run the dynamo

model to simulate the solar cycle. However, when we use the observed BMR flux distribution with $\Phi_0 = 1$, we get decaying solutions for different parameters of the model. Runs A1–A2 in Table 1 represent these decaying solutions. Boosting the observed flux distribution even by a small factor does not help. We realized that when the flux distribution is increased at least by a factor of 28 (i.e., $\Phi_0 = 28$), we get a growing solution; see Runs A3–A4. The sustained dynamo action is easier if we add a downward magnetic pumping (γ_r); compare Run A3 with A5 and Run A4 with A6. Figure 4 displays time evolutions of magnetic fields for about 300 yr from Run A6, in which a surface magnetic pumping (γ_s) of 2 m s^{-1} is used. It is apparent that the magnetic field is stable and the overall cycle amplitude is limited in time. The dynamo saturation mechanism is the quenching of the tilt angle introduced through Equation (10). Because of this quenching, the mean tilt, shown by the dashed line in Figure 5(a), deviates from the actual Joy’s law: $\delta = \delta_0 \cos \theta$ (solid red line). We note that a recent coupled 2D \times 2D BL model of Lemerle & Charbonneau (2017) also produces a stable solution with the tilt quenching.

From the butterfly diagrams in Figure 4, we recognize that the magnetic field is largely dipolar because both the toroidal and radial fields are asymmetric across the equator. However, to make a quantitative measure of the equatorial symmetry of different components of the magnetic field, we compute the symmetric parity (SP) by cross-correlating the fields between two hemispheres in the same way as done in Chatterjee et al. (2004):

$$\text{SP}_j(r, \theta, t) = \frac{\int_{t-\frac{T}{2}}^{t+\frac{T}{2}} (B_j^N - \overline{B_j^N})(B_j^S - \overline{B_j^S}) dt'}{\sqrt{\int_{t-\frac{T}{2}}^{t+\frac{T}{2}} (B_j^N - \overline{B_j^N})^2 dt' \int_{t-\frac{T}{2}}^{t+\frac{T}{2}} (B_j^S - \overline{B_j^S})^2 dt'}}, \quad (11)$$

where j stands for the r , θ , or ϕ component; $B_j^N = \langle B_j(r, \theta, \phi, t') \rangle_\phi$, $B_j^S = \langle B_j(r, \pi - \theta, \phi, t') \rangle_\phi$, and overlines denote the average over period T . To identify the short-term temporal variation of the parity, we take $T = 3.73$ yr. In all the cases, we compute the parity at a fixed radius (at $0.72R$ for B_ϕ and R for B_r) and average over latitudes ($\pi/2 < \theta \leq \pi$). From the above definition of parity, we expect $\text{SP}_j = 1$ for a perfect symmetric field and -1 for an antisymmetric field. We note that for a dipolar field, $\text{SP}_r = -1$, $\text{SP}_\theta = 1$, and $\text{SP}_\phi = -1$, and the reverse is true for the quadrupolar field.

On taking the toroidal field at $r = 0.72R$ and the radial field at $r = R$ from Run A6, we compute the mean parity of the toroidal field $\text{SP}_\theta(t)$ and the mean parity of the radial field $\text{SP}_r(t)$. These quantities are displayed in Figure 6(d) for a few cycles. We observe that the parity of the bottom toroidal field is more antisymmetric than that of the surface radial field. The latter is largely deviated from the -1 mode due to continuous BMR eruptions at low latitudes. Thus if we had computed the parity of high latitudes B_r , then we would have obtained the value close to -1 (dipolar). When we compute the average parity over the whole simulation run, we obtain $\overline{\text{SP}}_r = -0.11$ and $\overline{\text{SP}}_\theta = -0.85$. The respective standard deviations of these parities are 0.23 and 0.22, suggesting that they have considerable deviations from their antisymmetric modes. These are seen in Figure 6(d), where parities tend toward the symmetric (quadrupolar) mode during solar maxima when new BMRs emerge on the surface. Then the decay of these

Table 1
Summary of the Simulation Runs

Run	Φ_0	σ_δ	η_{CZ} ($\text{cm}^2 \text{s}^{-1}$)	$\gamma_{\text{CZ}}, \gamma_{\text{S}}$ (m s^{-1})	\bar{B}_{tor} (kG)	\bar{B}_r (G)	Parity of B_ϕ [$\overline{\text{SP}}_\phi$ ($\sigma_{\text{SP}\phi}$, T_{SP})]	Period (yr)	# of BMRs (per cycle)	Variability of \bar{B}_r SSN
A1	1	0°	8.0×10^{10}	0, 0	subcritical
A2	1	0°	5.0×10^{10}	0, 0	subcritical
A3	28	0°	8.0×10^{10}	0, 0	58	310	−0.70 (0.30, 123)	9.0	3132	9% ...
A4	28	15°	8.0×10^{10}	0, 0	56	300	−0.77 (0.24, 125)	8.9	3157	11% ...
A5	16	0°	8.0×10^{10}	0, 2	67	300	−0.89 (0.18, 141)	9.4	3336	9% ...
A6	16	15°	8.0×10^{10}	0, 2	65	290	−0.85 (0.23, 143)	9.6	3374	11% ...
A6'	16	15°	8.0×10^{10}	0, 2	56	270	−0.70 (0.29, 142)	9.5	3188	10% ...
AB1	16	15°	8.0×10^{10}	0, 2	150	1000	+0.82 (0.20, 15)	7.6	33371	24% 4%
B1	1	15°	1.5×10^{12}	0, 0	subcritical
B2	170	15°	1.5×10^{12}	0, 0	390	8300	−0.92 (0.20, 165)	5.2	11981	14% 2%
B3	1	15°	1.1×10^{12}	0, 15	subcritical
B4	1	15°	1.5×10^{12}	4, 20	subcritical
B5	1	15°	1.0×10^{11}	2, 20	11	12	−0.67 (0.32, 296)	13.2	568	52% 59%
B6	1.5	15°	1.5×10^{12}	2, 35	8.5	37	−0.96 (0.13, 243)	14.9	1343	12% 19%
B7	1.3	15°	1.5×10^{12}	5, 25	6.8	21	−0.96 (0.10, 427)	11.2	994	18% 28%
B8	1.5	15°	1.5×10^{12}	10, 20	12	46	−0.89 (0.21, 317)	7.3	2420	40% 42%
B9	2.4	0°	1.5×10^{12}	2, 20	22	140	−0.98 (0.07, 1092)	10.5	3947	11% 14%
B10	2.4	15°	1.5×10^{12}	2, 20	30	190	−0.96 (0.10, 1465)	10.5	6052	35% 41%
B11	2.4	30°	1.5×10^{12}	2, 20	31	185	−0.90 (0.16, 4262)	10.8	6119	46% 54%
B12	3.4	15°	1.5×10^{12}	2, 20	38	190	−0.97 (0.08, 1162)	12.8	10817	17% 26%
B13	2.4	15°	1.5×10^{12}	2, 20	21	160	−0.94 (0.11, 734)	9.3	4366	23% 30%
C1	2.4	15°	1.5×10^{12}	2, 20	26	170	−0.94 (0.12, 493)	9.9	4641	26% 29%
D1	3.0	15°	1.5×10^{12}	2, 20	14	64	−0.90 (0.16, 1339)	13.9	1190	22% 31%

Notes. In the A series of simulations, the delay distribution of BMR eruptions is fixed (i.e., fixed τ_s and τ_p), but the observed flux distribution is scaled by the toroidal field at the base of the CZ, while in all other simulations the delay distribution is dependent on the magnetic field through Equation (12) but the flux distribution is fixed. Runs B12, B13, C1, and D1 are the same as Run B10, except in Run B12 B_{sat} is four times smaller and $\Phi_0 = 3.4$, in Run B13 η_i in the tachocline is same as that in the CZ, in Run C1 the quenching is in the BMR flux and not in the tilt, and in Run D1 different forms of magnetic-field-dependent τ_s and τ_p are used (see text). The rms values of the mean toroidal and poloidal fields over the entire computational domain are denoted by \bar{B}_{tor} and \bar{B}_r , respectively. Symbols $\overline{\text{SP}}_\phi$ and $\sigma_{\text{SP}\phi}$ respectively denote the mean and the standard deviation of the parity of $(B_\phi(0.72R, \theta, \phi))_\phi$ computed over T_{SP} yr of data. Periods are computed from the power spectra of the azimuthal-averaged toroidal field at $r = 0.72R$, integrated over 0°–30° latitudes for the A series of runs or from the yearly averaged sunspot number (SSN) for all other runs. In last two columns, the variabilities of the peak polar field (\bar{B}_r) and the peak SSN are measured as $\sqrt{\frac{1}{N} \sum_{i=1}^N (Q_i - \bar{Q})^2} / \bar{Q} \times 100\%$, where $Q = \text{peak } \bar{B}_r$ or peak SSN, $N = \text{total number of cycles}$, and $\bar{Q} = \frac{1}{N} \sum_{i=1}^N Q_i$. Runs A3–A6 and AB1 have spatial resolutions of $340 \times 512 \times 1024$ in r , θ , and ϕ , respectively, while all other runs, including A6', have resolutions of $200 \times 256 \times 512$.

BMRs produces largely antisymmetric (dipolar) fields at the solar minima. This is broadly consistent with observations (DeRosa et al. 2012).

Returning to Figure 4, we notice that this simulation also produces polarity reversals with an average period of 9.6 yr, equatorward migration of the toroidal field at low latitudes, and poleward migration of the radial field, all broadly consistent with observations.

As given by Equation (10), the tilt angle in this model has a random component following a Gaussian distribution with $\sigma_\delta = 15^\circ$ around Joy’s law. Because of this random component, the actual tilt angle in our model has a considerable variation. Since the poloidal field generated by the BL mechanism depends sensitively on the BMR tilt (Dasi-Espuig et al. 2010; Jiang et al. 2014; Hazra et al. 2017), its random scatter gives rise to cycle variability. This greatly enhances the relatively modest cycle variability arising just from the random time delay (MT16).

The variation of tilt angle has an even larger effect when the tilt acquires a “wrong” sign, that is, negative in the northern

hemisphere and positive in the southern hemisphere. The word “wrong” here is not intended as a value judgment. Rather, the “right” sign of a tilt is defined by Joy’s law. The random fluctuations can lead to a tilt that violates Joy’s law. This is the sense in which it is “wrong.” We note that having a wrong tilt does not necessary imply that the BMR violates Hale’s polarity rule. Wrong tilts happen frequently in our model, as seen in Figures 5 or 6(b), and produce a poloidal field of the opposite polarity. This is reflected in Figure 4(a) and more clearly in Figure 6(a), where we notice a mixed polarity field and frequent polar surges of opposite polarity. This type of mixed polar field is frequently found in observations; see, for example, Figure 8(a) of McIntosh et al. (2015). The radial polar flux density (flux per unit area) as shown in Figure 4(c) has a considerable cycle-to-cycle variation. The amount of variation is $\sqrt{\frac{1}{N} \sum_{i=1}^N (\bar{B}_{r_i} - \bar{B}_r^{\text{avg}})^2} / \bar{B}_r^{\text{avg}} \times 100\% = 12.2\%$ (where \bar{B}_r is the peak value of the radial flux density computed by averaging over 15° around the pole, $\bar{B}_r^{\text{avg}} = \frac{1}{N} \sum_{i=1}^N \bar{B}_{r_i}$, and $N = 34$, the total number of cycles).

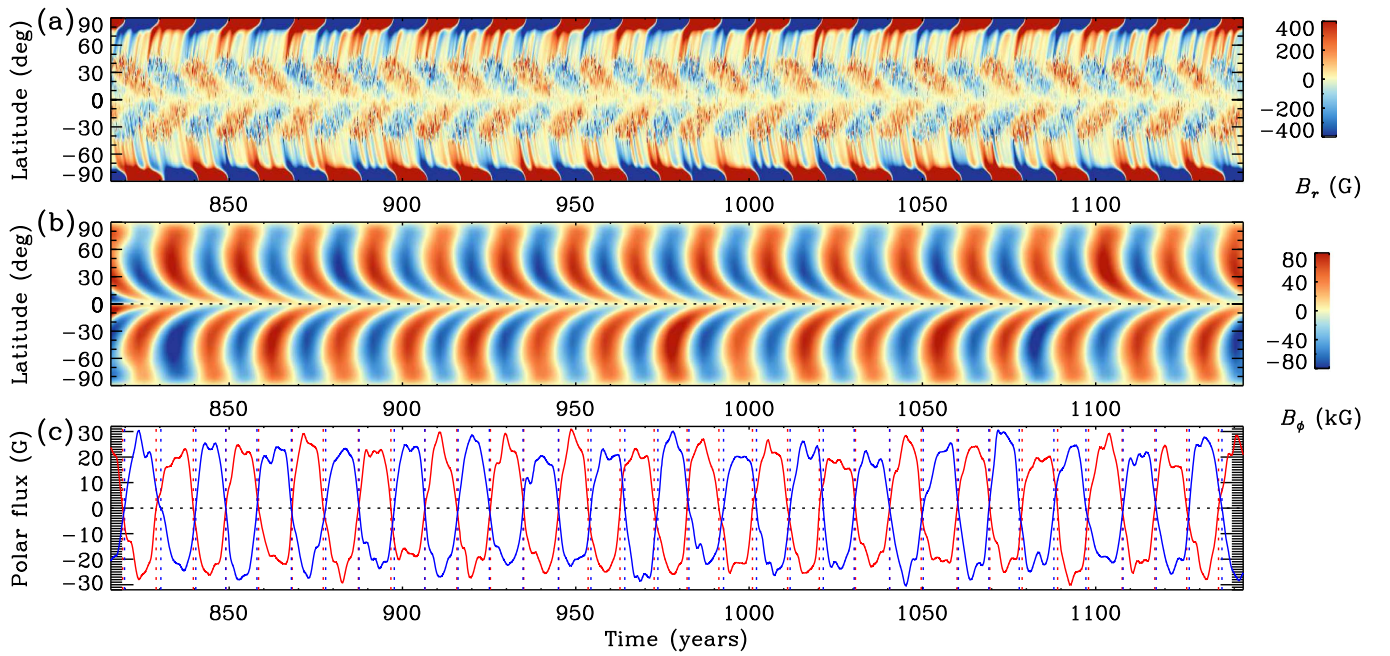


Figure 4. Results from Run A6: temporal evolutions of (a) the radial field $\langle B_r(R, \theta, \phi) \rangle_\phi$, (b) the toroidal field $\langle B_\phi(0.72R, \theta, \phi) \rangle_\phi$, and (c) the polar flux density, computed by averaging surface $(B_r)_\phi$ from 75° latitude to the pole (red: north, blue: south). The vertical dashed lines show the times of zeros of the mean polar flux. Note that the color scales in (a) and (b) are saturated at ± 400 G and ± 80 kG, while the extrema are $[-5.8, 5.9]$ kG and $[-90, 106]$ kG, respectively.

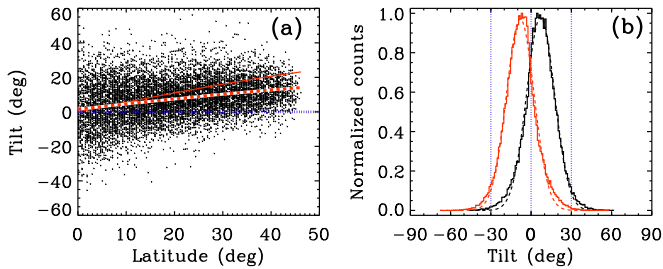


Figure 5. (a) BMR tilts vs. latitudes for the northern hemisphere. The solid, dashed, and dotted lines respectively show the actual Joy's law, $\delta = \delta_0 \cos \theta$, the linear fit of tilts, and the zero line. (b) Black and red are normalized histograms of tilts obtained from the northern and southern hemispheres, respectively. Dashed lines are the Gaussian fits with $\mu_\delta = 7^\circ$ and 8° , and $\sigma_\delta = 10.4$ and 10.3 (half width at half maximum HWHM = 12.3 and 12.2) for north and south, respectively. Vertical lines mark $\pm 30^\circ$ and 0° tilts. These plots are obtained from Run A6 presented in Figure 4, except in panel (a) where data only from years 850 to 875 are used.

The mean polar field in Figure 4(a) is larger than the observed value,² although the observed polar field is not reliably measured (because of the resolution limit and the projection effect). However, when we measure the mean polar flux density in high latitudes, say from 75° latitude to the pole as shown in Figure 4(c), we obtain a strength of the mean polar field around 20 G, which is close to the observed range. Another discrepancy between the present model and the observation is that there is a significant overlap between two cycles at each minimum; the cycle starts much before the end of its previous cycle (compare our Figure 4(a) with Figure 8(a) of McIntosh et al. 2015). The discrepancy can be attributed to our incomplete understanding of flux emergence and how to parameterize it with SpotMaker. Nevertheless, the overall morphology of our radial field resembles observations more closely than our previous model without tilt fluctuations

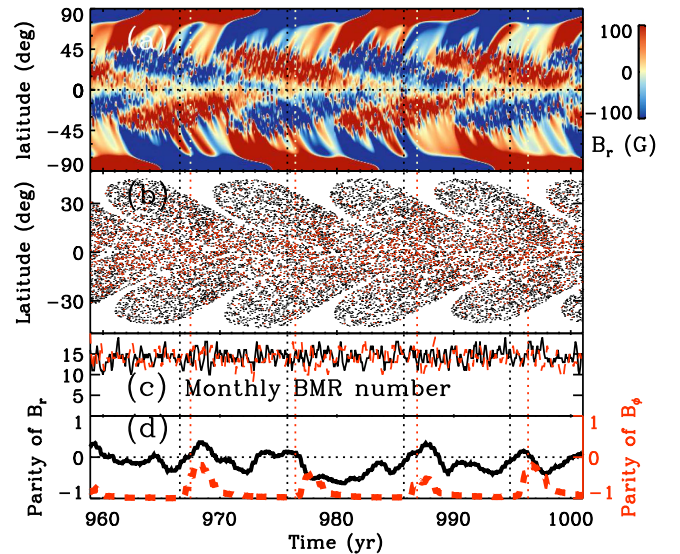


Figure 6. Temporal variations of (a) $\langle B_r(R, \theta, \phi) \rangle_\phi$, (b) BMR latitudes, (c) monthly number of BMRs (solid/dashed: north/south), and (d) SP_r and SP_ϕ (dashed) from Run A6 presented in Figure 4 but shown only for a few cycles. In panel (b), the red color shows BMRs with wrong tilts violating the sense of Joy's law, i.e., negative in the northern hemisphere and positive in the southern hemisphere. Vertical dotted lines show times of reversals of the low-latitude bottom toroidal flux; black/red: north/south. Note that the color scale in (a) is saturated at ± 100 G, while the maximum field strength is ± 5.5 kG.

(see MT16, for example) and also previous 2D dynamo models (Charbonneau 2010; Karak et al. 2014a).

We have demonstrated that in the present model, the cumulative effect of the short-term variations of the tilt angle is capable of producing a variation in the magnetic cycle, as seen in Figure 4(c). Thus we can conclude that a potential cause of solar cycle variability is the observed scatter of the tilt angle (Stenflo & Kosovichev 2012; Senthamizh Pavai et al. 2015; Wang et al. 2015). While we in our 3D dynamo model

² See <http://solarscience.msfc.nasa.gov/images/magbfly.jpg>.

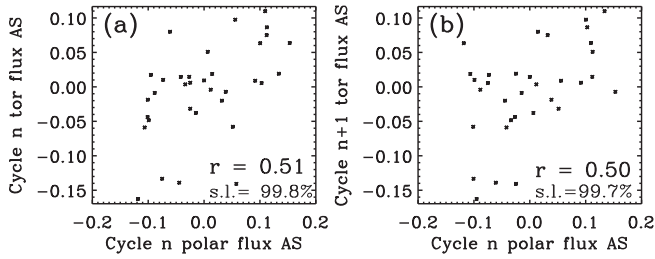


Figure 7. Results from Run A6: scatter plots between the asymmetry of the peak surface polar flux and the asymmetry of the peak toroidal flux at the base of the CZ for (a) the same cycle and (b) for the next cycle.

and Lemerle & Charbonneau (2017) in their coupled $2D \times 2D$ model explicitly demonstrate this, the original idea was known since the work of Charbonneau & Dikpati (2000). Recently, Cameron et al. (2013) demonstrated this idea using observations, while Jiang et al. (2014) for the first time quantified the effect of the tilt scatter on the polar field using an SFT model. Based on this idea, many authors (e.g., Yeates et al. 2008; Choudhuri & Karak 2009; Oleson & Kitchatinov 2013) modeled irregular features of the solar cycle by including fluctuations in the BL α term of their 2D flux transport dynamo models.

We mention that fluctuations of BMR tilts in our model were approximated by a Gaussian distribution with $\sigma_\delta = 15^\circ$. In observations, however, there is large scatter near the two tails of the distribution that is not captured in our Gaussian model; compare our Figure 5(b) with Figure 2 of Wang et al. (2015) or Figure 12 of Senthamizh Pavaai et al. (2015). Thus, in our model, if we had considered the tilt angles from the actual observations, then we would have achieved even more variation in the magnetic field than we have obtained here.

Though the dynamo maintains a strong hemispheric coupling, it also exhibits a noticeable hemispheric asymmetry (Figure 4(c)). Thus we find nonzero values for the asymmetry in peak surface polar fluxes, as measured by $AS_{pol} = (|\bar{B}_r^N| - |\bar{B}_r^S|) / (|\bar{B}_r^N| + |\bar{B}_r^S|)$. We note that this is not the parity of the polar field computed in Equation (11). If there were no asymmetry introduced in the poloidal flux generation, then the asymmetry in the toroidal flux would be reflected in the poloidal flux, and we would have obtained a strong correlation between these two. Nonetheless, we find only a moderate correlation (with linear Pearson correlation coefficient $r = 0.51$ with a significance level $((1-p) \times 100\%)$ of 99.8%) between the polar flux asymmetry and the low-latitude toroidal flux asymmetry (AS_{tor}); see Figure 7(a). This suggests that the asymmetry in the toroidal flux is not the only cause of the asymmetry in the poloidal flux; rather it can be produced from the asynchronous BMR emergence rate and the tilt angle. The asymmetric polar flux should eventually cause an asymmetry in the toroidal flux. However, due to hemispheric coupling at the equator, the asymmetry gets reduced over time, and we find a moderate correlation between the asymmetry in the polar flux and the asymmetry in the next cycle toroidal flux, as shown in Figure 7(b).

As discussed in Section 2, when we do not have sufficient spatial resolution, the sizes of the smallest BMRs are limited by the spatial grid size. In Run A6, the minimum size of BMRs is about 6.8 Mm. The number of BMRs below this size is very small, and thus the net flux from these small BMRs is negligible in the poloidal field generation. Hence, the spatial resolution of this simulation ($340 \times 512 \times 1024$) is sufficient

to capture the observed BMR spectrum. However, when we reduce the resolution to $200 \times 256 \times 512$, then the sizes of the smallest BMRs are about 13.6 Mm. Thus this resolution is not adequate to resolve the full BMR spectrum, and therefore we find a noticeable difference in the dynamo solution; see Run A6' in Table 1 for this simulation. Although the morphologies of the magnetic fields (not shown) are not too different in comparison to Run A6, we find considerably smaller values of the magnetic fields. The reason for the weaker field could be the following. In comparison to Run A6, in Run A6' the sizes of the smallest BMRs are larger but the BMR field strengths are smaller. Thus, in Run A6', most of the flux from these smallest BMRs gets easily canceled out, and less flux is able to reach to higher latitudes. This causes a weaker magnetic field in Run A6'. Furthermore, the values of \overline{SP}_p and \overline{SP}_o are different (-0.14 and -0.70 are the values, respectively, in comparison to -0.11 and -0.85 for Run A6). Thus the parity of the dynamo solution is slightly sensitive to how we resolve the small BMRs.

4. Cycle-dependent BMR Emergence Rate

In the calculations presented in Section 3, the time delay is computed from a log-normal distribution given by Equation (7) with fixed τ_s and τ_p . Hence as long as the spot-producing toroidal field exceeds the threshold field strength, the eruption can happen almost equally over the whole cycle. This contributes to the significant overlap between successive cycles, as seen in Figure 6. Well before the end of a cycle, emergences from the next cycle start, and we do not observe a noticeable cyclic variation in the BMR number; see Figure 6(c). One potential cause of this problem is that we have chosen a fixed time delay distribution over the entire cycle, which is unlikely to be true. In observations, we find more BMRs during solar maxima than during minima; see the thick and the thin solid lines in Figure 2. From these data, we estimate that, during a solar minimum, the mean time delay τ_s (and mode τ_p) of BMR appearance is about 10 days (and 1 day). However, as we go toward a solar maximum, the emergence becomes more frequent, and the mean time delay can be as short as a day. Motivated by this observed feature, we make τ_p and τ_s as the toroidal magnetic energy dependent such that in the northern hemisphere

$$\tau_p = \frac{2.2 \text{ days}}{1 + (B_b^N/B_\tau)^2}, \quad \tau_s = \frac{20 \text{ days}}{1 + (B_b^N/B_\tau)^2}, \quad (12)$$

where B_b^N is the azimuthal-averaged toroidal magnetic field in a thin layer from $r = 0.715R$ to $0.73R$ around 15° latitudes, and the value of B_τ is tuned to 400 G such that we get roughly the same number of BMRs as in observations. For the southern hemisphere, we have the same expressions for τ_s and τ_p , relating to the toroidal field in that hemisphere. In this way, no hemispheric synchronization is made in the waiting time of the BMR appearance, which is physical. We note that Lemerle & Charbonneau (2017) also used a magnetic-field-dependent delay in the BMR emergence through an emergence function, although their number of new BMRs at every numerical time step is extracted from a uniform distribution; see their Section 2.4.2.

We repeat the previous simulation, Run A6, using the delay distribution with modified τ_s and τ_p as given in Equation (12) and no other changes. This new simulation is labeled as Run AB1 in Table 1, and the result is displayed in Figure 8. The most distinct result we find from this simulation is that the initial dipolar field is flipped to a quadrupolar field in about 150 years. The mean parity of the bottom toroidal field over the

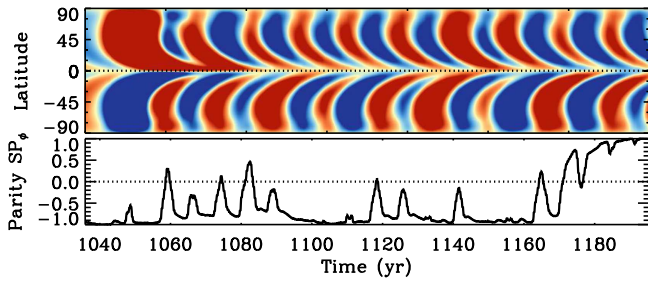


Figure 8. Temporal evolutions of $\langle B_\phi(0.72R, \theta, \phi) \rangle_\phi$ (top) and the parity of this field (bottom), obtained from Run AB1, which was started from the dipolar field of Run A6 and eventually settled to a quadrupolar solution.

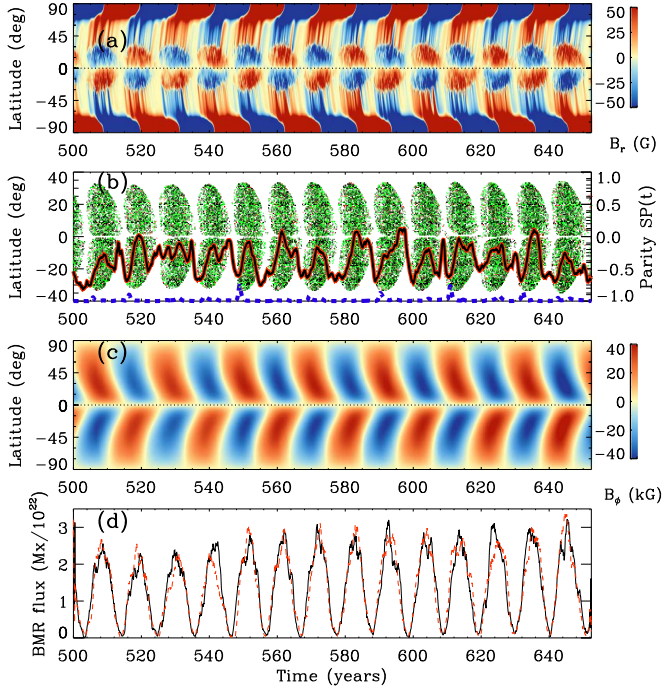


Figure 9. Results from Run B9: temporal variations of (a) $\langle B_r(R, \theta, \phi) \rangle_\phi$, (b) latitudes of BMRs, (c) $\langle B_\phi(0.72R, \theta, \phi) \rangle_\phi$, and (d) daily BMR fluxes in $Mx/10^{22}$ (black/red: north/south) produced by this model. In (b), points with different colors represent different sizes of BMRs. Green, black, and red correspond to BMRs of areas < 500 Mhem (millionth of a solar hemisphere), $500 \text{ Mhem} \leq \text{areas} < 1000 \text{ Mhem}$, and areas $\geq 1000 \text{ Mhem}$, respectively. In the same panel, the black/red and blue dashed lines show parities, $SP(t)$ computed over the four years of surface B_r and the bottom B_ϕ , respectively.

whole simulation becomes -0.46 , while for the last 15 years it is $+0.82$. Thus when we make the BMR delay dependent on the magnetic field, the quadrupolar mode is preferred over the dipolar mode. This suggests that both the dipolar and quadrupolar modes have comparable growth rates, and both modes can readily be excited with relatively minor changes in the simulation parameters. We return to this issue in Section 4.1 below. Another point to note in Figure 8 is that the overall dynamo efficiency is larger and the cycle period is shorter than in the previous case of a fixed delay distribution. The reason is not difficult to understand. Once the toroidal field at the base of CZ is stronger, it reduces τ_s and τ_p to make the BMR eruption more frequent. This frequent eruption makes the poloidal field production faster, which ultimately causes the stronger fields and faster polarity reversals.

4.1. Diffusion-dominated Regime

4.1.1. Steady Dynamo Solution

We recall that in the previous models, the bulk diffusivity η_{CZ} was taken to be $8 \times 10^{10} \text{ cm}^2 \text{ s}^{-1}$, which is much smaller than the surface diffusivity ($\eta_s = 3 \times 10^{12} \text{ cm}^2 \text{ s}^{-1}$). Previous studies from 2D BL models have demonstrated that a weaker diffusion promotes quadrupolar parity (Dikpati & Gilman 2001; Chatterjee et al. 2004; Hotta & Yokoyama 2010). Thus, we increase η_{CZ} to a much larger value of $\sim 10^{12} \text{ cm}^2 \text{ s}^{-1}$. Unfortunately, at this higher value of η_{CZ} , we do get a decaying solution (Run B1). One way to get a stable solution is to shift the observed flux distribution toward larger values (i.e., $\Phi_0 > 1$). The cycle period then becomes unrealistically short; see Run B2 in Table 1.

Karak & Cameron (2016) have shown that a downward pumping near the surface reduces the diffusion of the flux across the surface and helps to achieve a dynamo at a higher value of η_t than hitherto. However, even with a reasonable amount of surface pumping, we tend to get decaying solutions unless we increase the observed flux distribution by a small value; see Runs B3–B4. Obviously, the dynamo is efficient if we reduce η_{CZ} significantly; see Run B5. Thus by increasing the observed flux distribution by a small amount and using a surface pumping of about 20 m s^{-1} , we get growing solutions for $\eta_{CZ} > 1 \times 10^{12} \text{ cm}^2 \text{ s}^{-1}$; see Runs B6–B11.

Comparing Runs B2, B6, and B10, we notice that the cycle period increases with the increase of surface pumping γ_s . This is expected from the study of Karak & Cameron (2016), that the pumping makes the dynamo efficient and thus allows us to use a smaller value of Φ_0 . This makes the period longer by regulating the strength of the BL α effect. However when the pumping in the whole CZ is increased, the downward transport of the poloidal field becomes more efficient, reducing the time lag between poloidal and toroidal field conversion. That is the reason for getting a shorter period at a stronger γ_{CZ} in Run B8.

Results from Run B9 with $\eta_{CZ} = 1.5 \times 10^{12} \text{ cm}^2 \text{ s}^{-1}$ and with no fluctuations around Joy's law are shown in Figure 9. We note that in addition to changes in η_{CZ} , γ_{CZ} , and γ_s , two more changes have been made in this B series of simulations and Runs C1–D1. First, the meridional circulation profile has also been changed. To enhance the efficiency of the toroidal flux advection in this diffusion-dominated model, we made the meridional flow speed near the base of the CZ faster than in the previous advection-dominated model (Runs A1–A6 and AB1). The latitudinal component of this flow is shown by the solid line in Figure 1(a). This new meridional flow is produced from the same analytical profile as used in the previous advection-dominated model, which is the same as in Karak & Cameron (2016), except the prefactor $(r-R_p)$ in their Equation (5) for the stream function is removed and the surface flow speed is adjusted to 20 m s^{-1} . Second, the spot-producing toroidal flux is computed in the tachocline; that is, $r_a = 0.7R$ and $r_b = 0.715R$ are taken in Equation (5).

Interestingly, in this diffusion-dominated model, the mean parity of the bottom toroidal field SP_ϕ is -0.98 . Thus the toroidal field is largely antisymmetric across the equator (Figure 9) with minimal variation in the parity (with standard deviation of $SP_\phi = 0.07$). However, the mean parity of $B_r(R, t)$, shown by the black and red line in Figure 9(b), deviates most strongly from the antisymmetric (dipolar) mode during cycle maxima. This is consistent with the analysis of

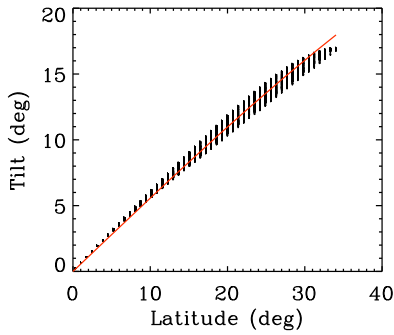


Figure 10. Tilts of the northern hemisphere BMRs from Run B9 as functions of latitudes. The red line represents the standard Joy’s law: $\delta = \delta_0 \cos \theta$.

solar data by DeRosa et al. (2012), namely that the parity of the observed radial magnetic field is dipolar during a solar minimum but becomes quadrupolar during a solar maximum because of the emergence of many BMRs.

Our simulation also produces most of the other features of the solar cycle. However, there are some differences seen in this simulation compared to the previous advection-dominated model. The tilt quenching, which produces the stable solution, is much weaker than in the previous model; see Figure 10. This small amount of quenching is sufficient to halt the dynamo growth. Thus, the observational signature of tilt angle quenching may be subtle, and the weak evidence in favor of it (Dasi-Espuig et al. 2010; Stenflo & Kosovichev 2012) may be sufficient to rank this as a viable candidate for dynamo saturation.

Noticeably, the overlap between two cycles at the minimum has now been reduced significantly compared to the cases with lower diffusion (Figure 4). Importantly, now we do not need to increase the observed flux distribution by a large value to achieve sustained dynamo action; here $\Phi_0 = 2.4$. The amount of daily flux produced by the model with this value of Φ_0 (Figure 9(d)) is comparable to the observed BMR flux budget (e.g., Schrijver & Harvey 1994; Zhang et al. 2010; Li 2017). Moreover, the average number of BMRs per cycle in this simulation is 3947, which is very close to the observed group sunspot number (3461) obtained from the catalog of RGO and USAF/NOAA sunspots averaged over the last 12 cycles (counting each spot only once). Thus this is the first 3D solar dynamo model that is totally sustained by the observed distribution of tilted BMRs.

The magnitude of the magnetic pumping needed to sustain the dynamo (for example, 35 m s^{-1} for $\Phi_0 = 1.5$ in Run B6) is reasonable since it is still only a small fraction of the observed velocity amplitude of $1\text{--}2 \text{ km s}^{-1}$ that characterizes solar surface convection (Nordlund et al. 2009). Notably, for the same value of diffusivity, our model uses less pumping to sustain an 11-year dynamo cycle than the previous 2D BL model of Karak & Cameron (2016); see their Figure 16. The possible reason could be the minor differences in the other parameters and the implementation of the BL process (explicit BMR deposition versus α coefficient).

We recall that the frequency of BMR emergences is governed by a delay distribution of the type given in Equation (7). This produces a much more realistic variation of the surface BMR flux, as shown in Figure 9(d). Also the sunspot number (SSN) goes up and down with time in a fashion similar to the real sunspot cycle; see Figure 11. We remember that this is the actual SSN produced by the model,

and it is not a proxy. In all previous dynamo models (e.g., Charbonneau & Dikpati 2000; Jiang et al. 2007; Olemskoy & Kitchatinov 2013; Passos et al. 2014), except the one of Lemerle & Charbonneau (2017), a proxy of SSN is constructed based on the integrated toroidal field near the base of the CZ. Ours is the first 3D solar dynamo model to explicitly produce a spontaneously generated distribution of BMRs that varies with the phase of the magnetic cycle.

The asynchronous time delay of BMR emergence and the asynchronous flux distribution within two hemispheres is sufficient to produce a considerable hemispheric asymmetry in the magnetic field and also in the BMR flux (Figure 9). The hemispheric asymmetry produced in this model is not large and gets corrected in one or two cycles. This is expected because the diffusive coupling between two hemispheres at the equator helps to reduce the hemispheric asymmetry. Furthermore, the stochastic process involved in the BMR emergence causes occasional spikes at any phase of the solar cycle and sometimes causes double peaks in some cycles (e.g., around 605 years and 645 years in Figure 9(d)). Hemispheric asymmetry can also contribute to double peaks (see Figure 15 below). Similar behavior is seen in many observed solar cycles (McIntosh et al. 2013).

Despite the tilt angle quenching, the model produces an observable variation in the amplitude of the cycle. This is particularly seen in the daily BMR flux of Figure 9(d) and in the monthly SSN (Figure 11). The amount of variation in the peak monthly SSN is $\approx 14\%$. We recall that in this model there is no randomness in the tilt angle around Joy’s law. Thus we need to consider what other factors give rise to the cycle variability.

We address this issue with the schematic diagram shown in Figure 12. In the BL process, decay and dispersal of tilted BMRs on the solar surface produce a poloidal field at the end of the cycle. Thus we expect the polar flux of a cycle to depend on the amount of flux that has emerged in BMRs during that cycle, and we expect these two quantities to be highly correlated. However, we get a linear correlation coefficient of less than one; see the second row in Table 2 for all correlations. The reason behind the reduction of the correlation is the nonlinearity in the tilt angle, which reduces the tilt when the BMR field exceeds B_{sat} . This nonlinearity is shown by the first vertical arrow in Figure 12. The variation in the mean BMR latitudes also has some effect on the process: BMR (n) \rightarrow poloidal flux (n), although in this simulation there is not much variation in it, and we ignore it in the discussion.

The poloidal field produced on the solar surface is transported to the deep CZ, where differential rotation produces a toroidal field for the next cycle. Thus the process poloidal flux (n) \rightarrow toroidal flux ($n+1$) is fully deterministic. The next process, toroidal flux ($n+1$) \rightarrow BMR ($n+1$), however, is not fully deterministic because both the BMR time delay and BMR flux are taken randomly from their distributions. These sources of randomness are indicated by the second vertical arrow in Figure 12. However, they largely average out over many BMRs, otherwise we would not get a strong correlation between the polar flux (n) and the BMR flux ($n+1$), as listed in Table 2. This is in agreement with the correlation obtained from the observed polar field data (Choudhuri et al. 2007) and from different proxies of the polar field (Muñoz-Jaramillo et al. 2013; Priyal et al. 2014). In fact, this correlation is a popular basis for the solar cycle prediction (Schatten et al. 1978).

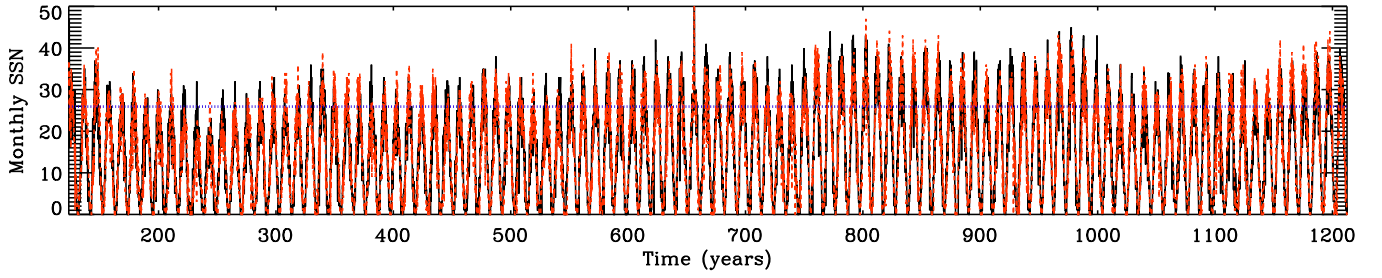


Figure 11. Time series of the BMR number from the simulation presented in Figure 9 but highlighting a longer time interval. The horizontal line shows the mean of peaks of the monthly BMRs obtained for the last 13 observed solar cycles.



Figure 12. Schematic diagram of our BL dynamo model with nonlinearities and randomness involved in it (see text for discussion). Here n refers to the cycle number.

Table 2

Summary of the Linear Pearson Correlation Coefficients and the Percentage Significance Level (s.l. = $(1 - p) \times 100\%$) between the Polar Flux of Cycle n and the BMR Flux (or the Spot-producing Bottom Toroidal Flux in the Case of Run A6) of the Subsequent Cycles

Description of Run	Correlation between pol. flux (n) and	Value (s.l. %)
Advection-dominated, and fluctuations in tilt (Run A6)	tor. flux (n)	0.18 (56.9)
	tor. flux ($n+1$)	0.64 (99.9)
	tor. flux ($n+2$)	-0.23 (78.6)
	tor. flux ($n+3$)	-0.19 (49.8)
Diffusion-dominated, and no fluctuations in tilt (Run B9)	BMR flux (n)	0.79 (99.9)
	BMR flux ($n+1$)	0.88 (99.9)
	BMR flux ($n+2$)	0.77 (99.9)
	BMR flux ($n+3$)	0.66 (99.9)
Same as Run B9 but with fluctuations in tilt (Run B10)	BMR flux (n)	0.87 (99.9)
	BMR flux ($n+1$)	0.97 (99.9)
	BMR flux ($n+2$)	0.84 (99.9)
	BMR flux ($n+3$)	0.75 (99.9)
Same as Run B10 but four times weaker B_{sat} (Run B12)	BMR flux (n)	0.37 (99.8)
	BMR flux ($n+1$)	0.86 (99.9)
	BMR flux ($n+2$)	0.25 (95.5)
	BMR flux ($n+3$)	0.00 (21.0)
Same as Run B10 but diffusivity in the tachocline is same as the value in the CZ (Run B13)	BMR flux (n)	0.71 (99.9)
	BMR flux ($n+1$)	0.91 (99.9)
	BMR flux ($n+2$)	0.58 (99.7)
	BMR flux ($n+3$)	0.41 (93.5)

We must remember that although the polar flux (n) and thus the toroidal flux ($n+1$) are positively correlated with the BMR flux ($n+1$), the process may not be linear. In our model, the BMR delay distribution involves a nonlinearity: it produces more BMRs when the toroidal flux at the base of the CZ is stronger. This nonlinearity is identified by the third arrow in Figure 12.

From the above analysis, we realize that the causes of the magnetic cycle variation in this model are the nonlinearities in tilt angle and in the delay distribution and the randomness in

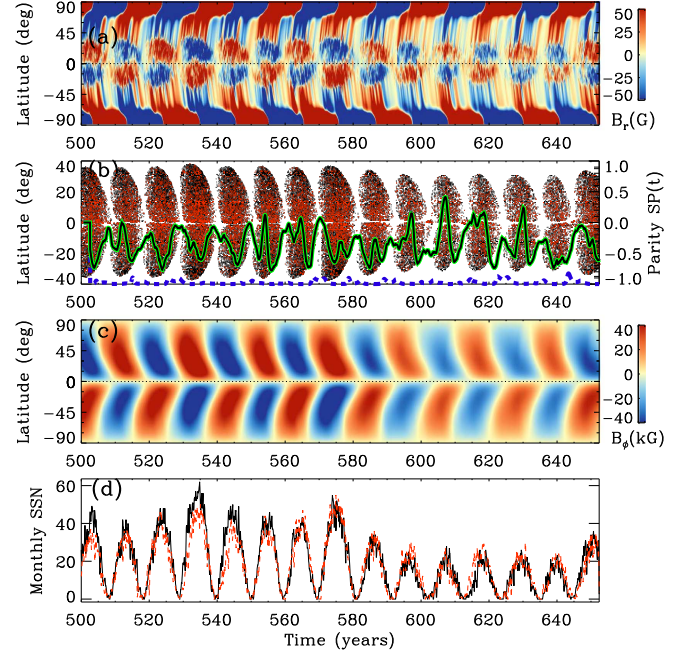


Figure 13. Results from Run B10: temporal variations of (a) $\langle B_r(R, \theta, \phi) \rangle_\phi$, (b) latitudes of BMRs, (c) $\langle B_\phi(0.72R, \theta, \phi) \rangle_\phi$, and (d) the monthly smoothed SSNs; black/red: north/south. In (b), red points show the wrongly tilted BMRs; green solid and blue dashed lines show parities, $SP(t)$ computed over the four years of surface B_r and the bottom B_ϕ , respectively.

the BMR emergence process. As discussed above, the randomness in the BMR emergence has a minor contribution to the cycle variation, although it is difficult to separate out the contributions of each component.

4.1.2. Solution with Observed Tilt Angle Fluctuations

In the above model, we now include variation in the tilt angle as guided by the observations, that is, a Gaussian fluctuation with $\sigma_\delta = 15^\circ$ around Joy's law (Equation (10)). Run B10 in Table 1 refers to this case. A few cycles from this stochastically driven dynamo simulation are presented in Figure 13, while the sunspot time series from the full simulation is shown in Figure 14. Comparing Figure 13 with Figure 9, we notice a greater variation in the magnetic field. Particularly, in Figure 13(a) we observe a frequently mixed polarity field as a consequence of the wrong tilt. The cycle-to-cycle variation of the amplitudes of the mean polar flux is $\sqrt{\frac{1}{N} \sum_{i=1}^N (\bar{B}_{r_i} - \bar{B}_r^{\text{avg}})^2} / \bar{B}_r^{\text{avg}} \times 100\% \approx 35\%$ (where $N=93$). This value is in agreement with Jiang et al. (2014), who found

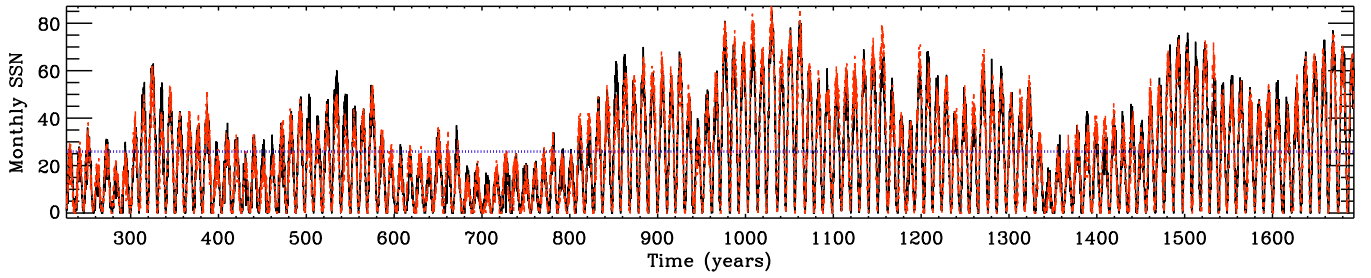


Figure 14. Monthly BMR number (smoothed over three months) with time. This is obtained from Run B10, which is displayed in Figure 13, but after running it for a longer time. The dotted line shows the mean of the observed peak SSNs for the last 13 cycles.

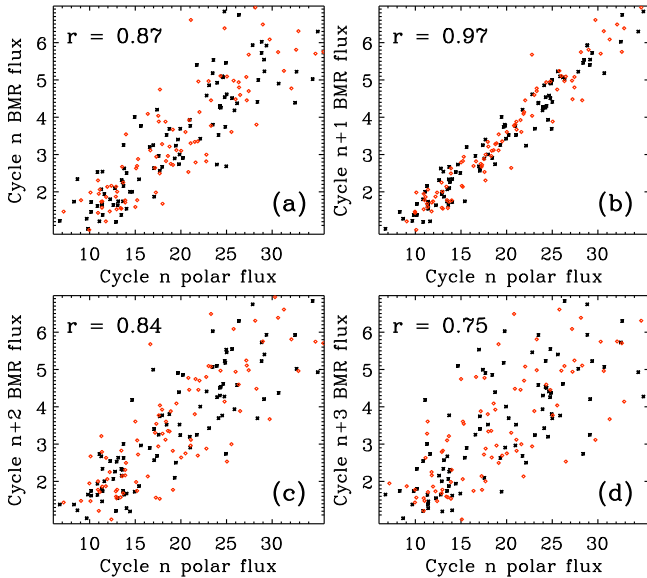


Figure 15. Scatter plots between the polar flux density (G) of cycle n and the daily BMR flux (in units of 10^{22} Mx) of (a) cycle n , (b) cycle $n + 1$, (c) cycle $n + 2$, and (d) cycle $n + 3$ from Run B10. Significance levels of all correlations are above 99.9%. Two different symbols correspond to two different hemispheres.

about 30% variation for cycle 17 in the axial dipole moment and the polar field compared to the value without tilt scatter.

The strength of the magnetic field and the number of BMRs per cycle have increased in this simulation with respect to the simulation without tilt fluctuations (Run B9); see Table 1. The reason for this will be explored later. The amount of variation in the peak SSN is $\sqrt{\frac{1}{N} \sum_{i=1}^N (PSN_i - \overline{PSN})^2} / \overline{PSN} \times 100\% \approx 41\%$, while in the observed data (<http://www.sidc.be/silso/datafiles>) for 1749–2017, it is 32%. As the variation of the SSN in this model is much larger than that obtained from the model without tilt fluctuations, we can certainly conclude that the fluctuations in the flux emergence process and the nonlinearity in the BL process have a relatively minor effect on the variation of the magnetic cycle relative to the tilt angle scatter. Furthermore, this suggests that the observed tilt angle scatter in the Sun may be sufficient to account for the observed solar cycle variability.

The basic dynamo loop shown in Figure 12 still applies for this model but with the inclusion in the process of a randomness due to tilt scatter: BMR (n) \rightarrow polar flux (n). Interestingly, we still find a fairly good correlation ($r = 0.87$) between the BMR flux (n) and the polar flux (n); see Figure 15(a). Using the polar faculae as a proxy for the polar

flux, Muñoz-Jaramillo et al. (2013) find a little correlation between the polar flux and the SSN of the same cycle. If their result is true, then it suggests that in the BL process of our model, the nonlinearity and randomness are weaker than in the real Sun.

As obtained from the previous model without tilt fluctuations, a strong correlation between the polar flux (n) and the BMR flux ($n + 1$) is expected, as shown in Figure 15(b). We remember that this correlation is very robust, and a similar correlation is obtained if we consider the peak SSN instead of the peak BMR flux. Moreover, a similar correlation is also obtained from the previous advection-dominated model; see Table 2. This is consistent with the idea that a reliable prediction of the future solar cycle is possible using the observed polar field of the previous solar minimum (Schatten et al. 1978; Choudhuri et al. 2007; Jiang et al. 2007).

As in the process BMR flux (n) \rightarrow polar flux (n), the correlation is not completely broken; the polar flux still has a correlation with the BMR flux ($n + 2$). This is shown in Figure 15(c). This correlation gets weakened in each transformation: poloidal flux (n) \rightarrow BMR ($n + 1$) \rightarrow poloidal flux ($n + 1$). Hence, we get a much weaker correlation between the polar flux (n) and BMR flux ($n + 3$).

Jiang et al. (2007) and Yeates et al. (2008) concluded that the memory of the polar flux is determined by the relative importance of diffusive and advective flux transport. In the diffusion-dominated model, they find one cycle memory between the polar flux and the toroidal flux, while in the advection-dominated it is three cycles. However, we find that the memory of the polar flux is not primarily related to the flux transport process; rather it is a fundamental consequence of any cyclic BL process. As explained through Figures 12 and 15, if the correlation between the BMR flux and the polar flux of the same cycle is not completely broken, then this correlation has to propagate for many cycles. This has happened in Figure 12 of Yeates et al. (2008), which they identify as the advection-dominated model. However, in Figure 11 of Yeates et al. (2008), the same cycle correlation has been broken, and they called this the diffusion-dominated regime. The broken correlation in their case is due to diffusion, while in our case it is due to both the nonlinearity in the BL process and the diffusion. This is confirmed by repeating the same simulation as shown in Figure 15 but reducing the B_{sat} of the tilt angle quenching in Equation (10) by four times (Run B12). The correlations between different cycles are listed in Table 2. As we can see from Equation (10) that when we keep everything else the same in the model but reduce B_{sat} , the nonlinearity in the model is effectively increased. This nonlinearity in the tilt angle acts to break the linear dependence between the polar flux and the BMR flux of the same cycle.

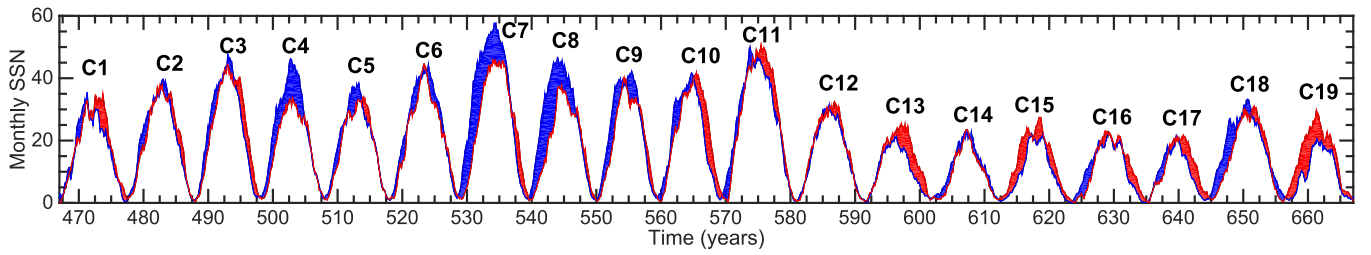


Figure 16. Portion of the smoothed SSN time series shown in Figure 14 with the red and blue lines showing the northern and southern hemisphere numbers, respectively. The shaded area represents the excess of the BMRs between two hemispheres. To facilitate the discussion, we have labeled the cycles.

One may think that a much weaker diffusivity in the tachocline has made our model more like the advection-dominated model and might be the cause of many cycle correlations in Figure 15. To check this, we have performed another simulation by increasing the tachocline diffusivity to $1.5 \times 10^{12} \text{ cm}^2 \text{ s}^{-1}$; that is, η_t in the tachocline is now the same as in the CZ (Run B13). No other changes are made in this simulation with respect to Run B10. Again in this simulation, we find similar values for correlations, as listed in the last row of Table 2. Stronger diffusion in the tachocline tries to reduce the correlation in each cycle but never diminishes it to one cycle, as we expect in the diffusion-dominated region.

We also mention that Karak & Nandy (2012) find a reduction of the memory in both advection- and diffusion-dominated dynamos to one cycle by the inclusion of a downward pumping. Actually, the pumping increases the strength of the magnetic flux and thus the nonlinearity, which reduces the memory to one cycle in Karak & Nandy (2012).

Thus, to summarize the whole idea, in the BL dynamo, as long as there is an efficient mechanism to transport the surface poloidal flux to the deep CZ, the polar flux and the BMR flux are cyclically coupled (Figure 12). If the nonlinearity in the BL process or the relative diffusive transport is sufficiently strong, then the memory of the polar flux will be limited to the next one cycle only, otherwise it will be propagated to multiple cycles.

Going back to the SSN plot in Figure 14, we observe some hemispheric asymmetry. In Figure 16, we highlight it for some cycles. In this figure, we clearly observe the temporal lag and the excess of BMRs between two hemispheres. We notice that the first three cycles in this figure are more or less symmetric. Then in cycle C4, the southern hemisphere got more spots, although the temporal symmetry is still retained. In the next cycle, the excess of spots in the southern hemisphere has now been reduced, and eventually in C6 it has diminished completely. Again in C7, a new asymmetry is introduced. But now the southern hemisphere has more spots, and this hemisphere is leading over the other in the rising phase. This is continued for the next two cycles. Then for C10–C13, the northern hemisphere has a few more spots, particularly during the decaying phase. C14 is very symmetric, while for C15, the northern hemisphere is a little longer than the other. Finally, for C18, the southern hemisphere is leading in the rising phase, while for C19, it is the opposite.

Certainly, we cannot make a one-to-one comparison of our sunspot cycles with the observed ones as we do not model the exact observed cycles. However, on comparing our sunspot cycles in Figure 16 with the observed cycles in Figure 10 of McIntosh et al. (2013), readers can convince themselves that very similar features of the solar cycle are reproduced in our model.

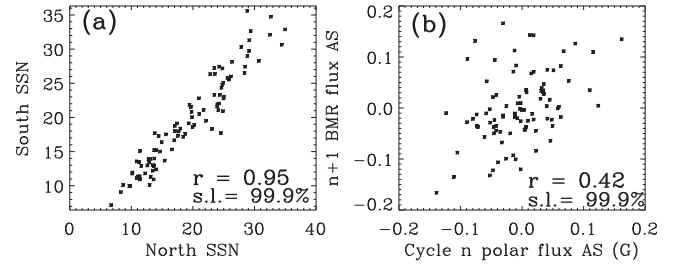


Figure 17. Scatter plots between (a) peaks of the northern SSN and the southern SSN, and (b) the normalized hemispheric asymmetry of polar flux of cycle n and the asymmetry of BMR flux of cycle $n+1$.

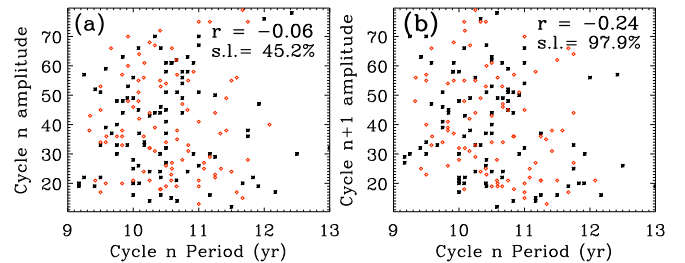


Figure 18. Scatter plots between periods and amplitudes of (a) the same cycles and (b) the next cycles. Two different symbols correspond to two different hemispheres.

We have seen in Figure 16 that, like the Sun, our model always tends to correct any (hemispheric or temporal) asymmetry produced in a cycle, and we do not observe extended asymmetry. Hence we obtain a strong correlation between the amplitudes of the north and the south sunspot cycles, as shown in Figure 17(a). The polar flux asymmetry obtained in this diffusion-dominated model is comparable to the value obtained from the previous advection-dominated model; compare the horizontal axes of Figures 17(b) and 7(a). However, the correlation between the polar flux asymmetry with the SSN asymmetry of the next cycle (Figure 17(b)) is much less than that found in the previous advection-dominated model. This is expected because in the diffusion-dominated model, fields are largely coupled across the equator, and much of the memory of the polar flux asymmetry is not preserved in the toroidal flux. Moreover, due to the asynchronous BMR emergence process, a new asymmetry is introduced (which is not related to the polar flux asymmetry).

In Figure 18(a) we show the scatter plot between the amplitudes and the periods. While in observations (Charbonneau & Dikpati 2000) there is a little anticorrelation, in our model we find almost no correlation. Interestingly, from the horizontal axis

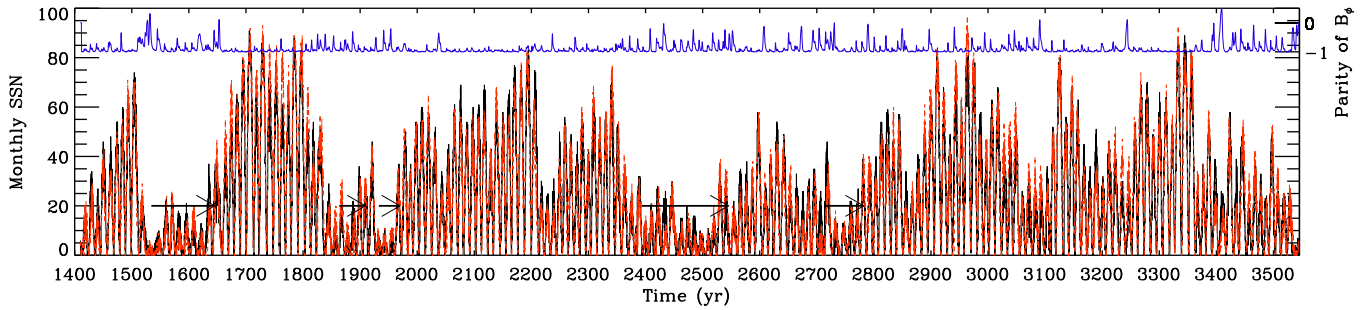


Figure 19. SSN time series (black/red: north/south) from Run B11, with $\sigma_\delta = 30^\circ$. The top blue line shows the evolution of the smoothed (over 11 years) parity $SP_\phi(t)$ of the bottom toroidal field. Arrows show the extent of grand minima based on our definition.

of this figure, we notice that the cycle period has considerable variation around its mean of 10.5 yr. In the flux transport dynamo paradigm, we believe that the cycle period is largely determined by the speed of the meridional flow (Dikpati & Charbonneau 1999), which is kept constant here. Thus the variation in our period is caused by the fluctuations and nonlinearities in the BMR emergence. Let us discuss how this is happening. When the polar field of a cycle becomes stronger due to the tilt fluctuations, spots in the next cycle take a longer time to reverse the previous cycle flux. This effect acts to make the cycle longer. However, there is another countereffect. A stronger polar flux makes the toroidal flux stronger, which leads to more frequent BMR emergence. This effect acts to reverse the polar flux quickly and makes the cycle period shorter, though it is inhibited by the tilt angle quenching. The competition between these two effects causes variation in the period.

Finally, we find a little anticorrelation between amplitudes and periods of previous cycles, as shown in Figure 18(b). In observations (see, e.g., Figure 4 of Hazra et al. 2015) this correlation is -0.67 , which is much larger than our value.

4.1.3. Grand Minima and Maxima

In Figure 14, we have seen that a random component following a Gaussian distribution with $\sigma_\delta = 15^\circ$ around Joy's law occasionally produces very weak and strong cycles and a few Dalton-like extended periods of weaker activity (e.g., around 700 years in Figure 14). Yet, the dynamo never becomes so weak as to produce any Maunder-like grand minimum. However, we must remember that for all BMRs we have considered the same level of tilt fluctuations, while in observations, there are indications that weaker BMRs have bigger scatter in their tilts (Stenflo & Kosovichev 2012; Jiang et al. 2014; Lemerle et al. 2015). Moreover, the tilt variation that we have implemented in the above simulations is extracted from the variation within data of a solar cycle (for example, cycle 23 in the analysis of Stenflo & Kosovichev 2012 and cycle 21 in the analysis of Lemerle et al. 2015). In observations (e.g., Dasi-Espuig et al. 2010; Wang et al. 2015; Arlt et al. 2016), we find the tilt to have cycle-to-cycle variation, in addition to variations within a cycle. Motivated by these observational results, we double the tilt fluctuations; that is, we now take $\sigma_\delta = 30^\circ$ instead of 15° . This simulation is labeled as Run B11, and the sunspot time series from this simulation is shown in Figure 19. Interestingly, again the dynamo does not shut off, and the cycle is still maintained even at this large tilt fluctuation. We find several episodes when the magnetic field

and the cycle become much weaker, for example, around 1600, 1900, and 2500 years. These events can be considered as Maunder-like grand minima.

To compute the number of grand minima and the time spent in those events, we follow the same procedure as applied in Usoskin et al. (2007). We first bin the data in 10-year intervals and then filter the data using Gleisberg's low-pass filter 1-2-2-1. We consider a grand minimum to occur when the SSN goes below 50% of the mean for at least two consecutive decades. Applying this procedure in the previous data set of Run B10 with $\sigma_\delta = 15^\circ$, we now get two grand minima (around times 1950 years and 2600 years). This simulation spent 9.3% of its time in these grand minima phases, which is much less than the value of 17% obtained in the ^{14}C data of Usoskin et al. (2007). This simulation also produces two grand maxima with time spent in these phases of 7.6%, which is again less than the value of 9% obtained in the ^{14}C data.

Ironically, the simulation of $\sigma_\delta = 30^\circ$ produces 26 grand minima in 11,400 years of the simulation run. Out of these 26 grand minima, five are shown by arrows in Figure 19. Our number of grand minima is very close to the value 27, obtained in the last 11,400 years of ^{14}C data (Usoskin et al. 2007). The time spent in the grand minima is 18%, which is again very close to the record from ^{14}C data. We are carrying out a detailed analysis of the grand minima, particularly how our model recovers from the grand minima phases, owing to a few BMRs. These will be presented in a forthcoming publication.

Our model also produces occasional periods of stronger activity resembling the solar grand maxima. In this simulation, we obtained 17 grand maxima, with time spent in these phases of 9.6%. Again these values are close to the ones obtained in the ^{14}C data. A detailed study of grand maxima will also be presented in the forthcoming publication.

On comparing Runs B9–B11 in Table 1, we notice that \overline{SP}_ϕ increases with the increase of the tilt angle scatter (σ_δ), that is, going toward the quadrupolar parity from the dipolar one. Also the deviation from the dipolar mode, as seen by the value of σ_{SP_ϕ} , increases with the scatter. It is not difficult to understand the reason. Due to scatter in the tilt, when a BMR gets a wrong tilt in one hemisphere, it produces a quadrupolar field instead of a dipolar field. The occurrence of this event increases with the increase of tilt scatter, and thus the parity tends to go to the quadrupolar parity. During grand minima when there are fewer BMRs, the effect of tilt fluctuations is more pronounced, and the deviation of the dipolar parity is significant, as seen in Figure 19.

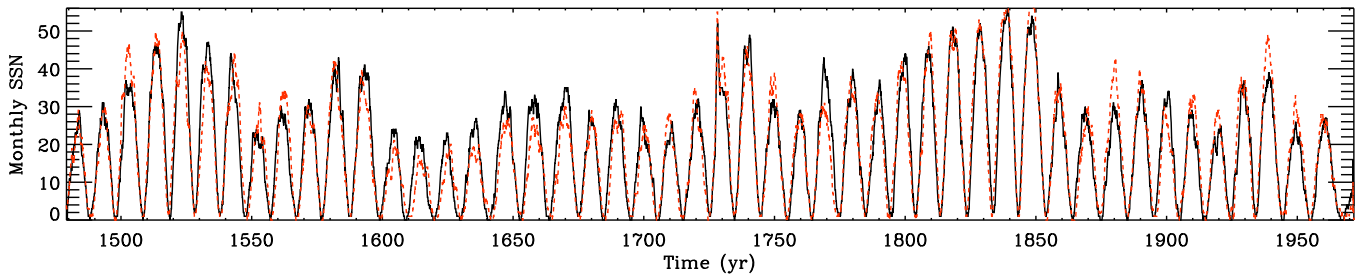


Figure 20. Same as Figure 14 (Run B10), but this is obtained from Run C1, in which the quenching is operating in the BMR flux and not in the tilt.

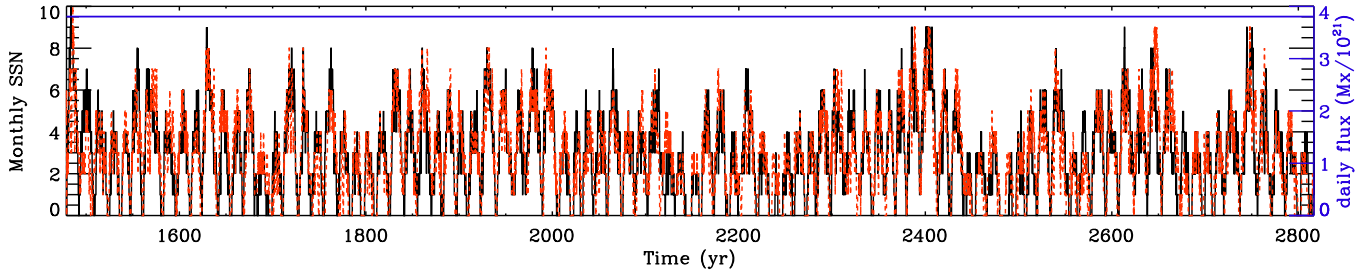


Figure 21. Same as Figure 14 (Run B10), but obtained from Run D1 in which the magnetic-field-dependent nonlinearity on the BMR delay is different; see Section 4.2 for details. The horizontal line shows the mean daily BMR flux (in the units of 10^{21} Mx) in this model.

4.2. Sensitivity of Solutions with Nonlinearities

To explore the sensitivity of the solar cycle variation with nonlinearities in the model, we consider Run B10 and perform the following two new simulations. First, instead of taking the nonlinear quenching factor $1/[1 + (\hat{B}/B_{\text{sat}})^2]$ in the tilt angle (which is the case in all previous simulations), we take it in the BMR flux. The Run C1 in Table 1 represents this case. Second, we keep the tilt quenching as before but change the magnetic-field-dependent factor $1/[1 + (B_b^N/B_\tau)^2]$ in Equation (12) for τ_p and τ_s to $1/(1 + B_b^N/B_\tau)$. Run D1 represents this case.

The result for Run C1 is shown in Figure 20. As listed in Table 1, the period and the number of BMRs per cycle are smaller in this simulation, although the morphology of the field (not shown) looks very similar to the previous simulation (Run B10). However, the variation of the peak SSN is 29%, which is somewhat smaller than in Run B10 (41%). It is surprising that when putting the same quenching factor from the tilt onto the flux, the model produces a different amount of variation in the solar cycle. The reason is that when the quenching is operating in the flux, the dynamo becomes more stable than when it is operating in the tilt. To clarify this point, we first estimate the magnetic field generated from only two symmetric BMR pairs deposited at $\pm 5^\circ$ latitudes at the beginning of a simulation. Tilts of these pairs are given by Joy's law, and no seed magnetic field is given in this simulation. (This study is very similar to the one presented in Section 4.2 of Hazra et al. 2017.) Then we perform two more simulations. In one, we reduce the flux of pairs by 50%, and in another, we keep the flux the same but reduce the tilt by the same amount. After running these simulations for about 5 yr, we find that the high-latitude radial flux in the former case has been reduced by about 64%, while in the latter case it is reduced by only 50%. Thus when the magnetic field tends to grow, it is easier for the dynamo to stabilize it by reducing the BMR flux than by reducing the same amount of tilt. This conclusion becomes even stronger by comparing values of \hat{B}_{tor} , \hat{B}_r , and the mean BMR number per cycle for Runs B10 and C1 in Table 1. We notice that all these values are smaller in

Run C1, confirming that the flux quenching did not allow the field to grow much.

Finally, we consider Run D1, which produces a decaying solution unless we increase the flux distribution by a small amount (see Table 1). The solution, in this case, shows a considerably different behavior. The overlap between cycles at the minimum has increased, and we do not observe very distinct cycles; see Figure 21. Moreover, the mean period becomes longer (14 yr instead of 10.5 yr as in Run B10), and the cycles are very irregular. This is expected because when decreasing the strength of the nonlinearity in τ_p and τ_s , the rate of spot production decreases, and thus the polarity reversal becomes slower. The most significant feature in this simulation is that the dynamo is still operating with only a few BMRs, although the BMRs are a little bigger (due to their larger flux). Thus \hat{B}_{tor} , \hat{B}_r , and the mean value of the daily BMR flux (the horizontal line in Figure 21) are also less compared to the previous Run B10. From this simulation, we can conjecture that this scenario might be applicable to other stars (probably the slowly rotating stars) that produce fewer BMRs and irregular and overlapped cycles. Another point to note is that the variation of the peak SSN in this simulation is less than in Run B10. We expect the variation to be larger due to the smaller number of BMRs, but because of having a less sensitive spot production rate with the magnetic field, the sunspot variation is reduced. From this simulation, we learn that with the decrease of the sensitivity of τ_p and τ_s with the magnetic field, the cycle-to-cycle variation in the peak SSN decreases slowly.

5. Summary and Conclusions

Using observed properties of the BMRs in our previous 3D BL solar dynamo model (MD14 and MT16), we have studied the behavior of the dynamo action and the causes of the variability of the magnetic cycle in this model.

We take the flux of BMRs from an observed distribution, and then we couple the net surface flux budget of BMRs with the toroidal field at the base of the CZ. We do this in two ways.

First, we scale the observed flux distribution based on the toroidal flux at the base of the CZ (Section 3). In this case, the delay distribution of BMR emergence is held fixed. Although the net BMR flux produced by this model has some variation with the magnetic cycle, the SSN does not show appreciable variation, due to a considerable overlap between two magnetic cycles at the minima (Figure 6).

In the second approach, we keep the observed flux distribution unchanged but vary the BMR emergence rate based on the toroidal flux at the base of the CZ (Section 4). Thus we get more BMRs at the solar maximum when the toroidal field is strong. As a result, we attain cyclic variations in the BMR flux and in the BMR number, in the same manner as we observe in the Sun. Thus for the first time in our model, we obtain a sunspot cycle that can be compared directly with observations, as opposed to using a proxy for this (e.g., Figure 11). Our main results are itemized below.

1. The overall dynamo growth is limited by a nonlinearity in the tilt angle. This is the only nonlinearity in the model when the time delay distribution is fixed.
2. Reduction of the tilt angle by only a few degrees is sufficient to limit the dynamo growth (Figure 10). Thus, potential signatures of tilt quenching in solar observations may be subtle.
3. When the BMR delay distribution is nonlinearly coupled with the toroidal flux, this nonlinearity acts counter to the tilt angle nonlinearity. In contrast to tilt nonlinearity, the delay nonlinearity acts to make the poloidal field strong by producing more BMRs when the toroidal field becomes strong. Thus the variation of the magnetic cycle in our model is controlled by the competition between these two nonlinearities.
4. These two nonlinearities, along with the randomness in the BMR emergence, are capable of producing a substantial variation in the magnetic cycle, as reflected by the SSN (Figure 9). A noticeable hemispheric asymmetry is also observed in this model.
5. The variability of the magnetic field is greater when the BMR delay distribution is dependent on the magnetic field; compare $\overline{B_r}$ from the A series of simulations with other simulations in Table 1.
6. When a scatter in the BMR tilt around Joy's law is included, the model produces a much larger variation in the magnetic cycle. The cycle variability in our simulations for $\sigma = 15^\circ$ ranges from 19% to 59%, depending on the flux transport (diffusion and pumping) and on the nonlinearities in the BMR emergence rate and tilt angles; see Table 1. The corresponding value for the Sun during 1749–2017 is 32%. So, within our BL paradigm, we find that the observed tilt angle scatter is sufficient to account for the observed solar cycle variability.
7. The simulation with the tilt saturation produces more variability than that with the flux saturation (compare Runs C1 and B10). Furthermore, the weaker diffusion in the CZ creates more variability (compare Runs B5 and B10).
8. The morphology of the magnetic fields in simulations with tilt scatters closely resembles observations. In particular, the surface radial field possesses a more mixed polarity field (Figures 6 and 13).
9. With the inclusion of tilt scatter, the north–south asymmetry in the magnetic cycle is increased

(Figure 16). However, the asymmetry never propagates for many cycles; through diffusion across the equator, the dynamo corrects this asymmetry within a few cycles. Similar behavior is also observed in the Sun (e.g., McIntosh et al. 2013).

10. Tilt scatter also triggers grand minima and grand maxima. The observed scatter of $\sigma = 15^\circ$ for the recent cycles is not sufficient to account for the grand minima inferred from cosmogenic isotopes (Usoskin et al. 2007). However, we do not include any positive feedback that might enhance the scatter. For example, weaker poloidal fields will produce weaker toroidal fields that will in turn produce weaker flux tubes with increased scatter due to buffeting by turbulent convection.
11. A larger scatter of $\sigma = 30^\circ$ leads to more frequent grand minima. For example, Run B11 spends 18% of its time in grand minima, compared to 17% for the Sun. A larger scatter also increases the time spent in grand maxima: 9.6% for Run B11 versus 9% for the Sun.
12. Our model never shuts down at the observed tilt fluctuations, which was the case in the recent model of Lemerle & Charbonneau (2017).
13. The scatter in the tilt angle makes the dynamo slightly weaker in simulations where the BMR delay distribution is fixed (compare Runs A3–A4 and Runs A5–A6). However, this is not true in the cases of magnetic-field-dependent delay distributions. The dynamo becomes even stronger with the increase of the tilt fluctuations; compare Runs B9–B11.
14. In all simulations, we do not vary the meridional flow with time, yet we observe some variation in the cycle period. Particularly, the simulation with tilt fluctuations of $\sigma_8 = 15^\circ$ produces a variation in the period that is indeed comparable to the observed solar cycle (Figure 18).

As demonstrated in a 2D flux transport dynamo model by Karak & Cameron (2016), we find that magnetic pumping enhances the efficiency of the dynamo. In particular, the inclusion of magnetic pumping allows us to achieve sustained dynamo solutions using a BMR flux distribution comparable to the observed distribution ($\Phi_0 < 3$), even in the diffusion-dominated regime (see the B series in Table 1). When magnetic pumping is not included, it is necessary to artificially boost the BMR flux ($\Phi_0 \gtrsim 28$) in order to achieve supercritical solutions (Runs A3–A4). Magnetic pumping also helps to make the magnetic field dipolar. The surface radial field, however, is largely dipolar (antisymmetric) only during the solar minimum, and it is dominated by the quadrupolar (symmetric) mode during the solar maximum when several BMRs emerge at the surface to produce a quadrupolar field (Figures 9 and 13(b)). This type of multipolar surface magnetic field is in agreement with solar observations (DeRosa et al. 2012). Our dynamo model, however, can flip from the dipolar mode to the quadrupolar mode even with small parameter changes (e.g., changes in the BMR delay distribution; Figure 8).

In our BL model, as the poloidal flux produces the toroidal flux and then this toroidal flux produces BMRs (Figure 12), the memory of the polar flux is largely reflected in the strength of the next sunspot cycle. We always obtain a strong correlation between the polar flux and the sunspots of the next cycle (Table 2). However, the memory of the polar flux may not be propagated to multiple cycles. Yeates et al. (2008), Jiang et al.

(2007), and Karak & Nandy (2012) have shown that the memory of the polar flux is limited by the relative importance of diffusive and advective flux transport. However, here we show that it is also determined by the nonlinearity in the BL process. When the nonlinearity in BMR tilt is strong, the memory of the polar flux is limited to one cycle, irrespective of the flux transport.

We thank the anonymous referee for offering many constructive comments that helped to improve the presentation. We are indebted to Lisa Upton for doing an internal review of this manuscript and for providing the observed data of the BMR delay distribution used in Figure 2. We extend our thanks to Arnab Rai Choudhuri for the discussion on the tilt angle fluctuations during Mark's visit to Bangalore. We are also thankful to Gopal Hazra and Mausumi Dikpati for discussions. B.B.K. is supported by the NASA Living With a Star Jack Eddy Postdoctoral Fellowship Program, administered by the University Corporation for Atmospheric Research. The National Center for Atmospheric Research is sponsored by the National Science Foundation. Computations were carried out with resources provided by NASA's High-End Computing program (Pleiades) and by NCAR (Yellowstone).

ORCID iDs

Bidya Binay Karak  <https://orcid.org/0000-0002-8883-3562>
Mark Miesch  <https://orcid.org/0000-0003-1976-0811>

References

- Arlt, R., Senthamizh Pavai, V., Schmiel, C., & Spada, F. 2016, *A&A*, **595**, A104
- Augustson, K., Brun, A. S., Miesch, M., & Toomre, J. 2015, *ApJ*, **809**, 149
- Babcock, H. W. 1961, *ApJ*, **133**, 572
- Belucz, B., Dikpati, M., & Forgács-Dajka, E. 2015, *ApJ*, **806**, 169
- Cameron, R., & Schüssler, M. 2015, *Sci*, **347**, 1333
- Cameron, R. H., Dasi-Espuig, M., Jiang, J., et al. 2013, *A&A*, **557**, A141
- Cameron, R. H., & Schüssler, M. 2016, *A&A*, **591**, A46
- Charbonneau, P. 2010, *LRSP*, **7**, 3
- Charbonneau, P. 2014, *ARA&A*, **52**, 251
- Charbonneau, P., & Dikpati, M. 2000, *ApJ*, **543**, 1027
- Chatterjee, P., Nandy, D., & Choudhuri, A. R. 2004, *A&A*, **427**, 1019
- Choudhuri, A. R., Chatterjee, P., & Jiang, J. 2007, *PhRvL*, **98**, 131103
- Choudhuri, A. R., & Karak, B. B. 2009, *RAA*, **9**, 953
- Dasi-Espuig, M., Solanki, S. K., Krivova, N. A., Cameron, R., & Peñuela, T. 2010, *A&A*, **518**, A7
- DeRosa, M. L., Brun, A. S., & Hoeksema, J. T. 2012, *ApJ*, **757**, 96
- Dikpati, M., & Charbonneau, P. 1999, *ApJ*, **518**, 508
- Dikpati, M., de Toma, G., Gilman, P. A., Arge, C. N., & White, O. R. 2004, *ApJ*, **601**, 1136
- Dikpati, M., & Gilman, P. A. 2001, *ApJ*, **559**, 428
- Dikpati, M., Gilman, P. A., Cally, P. S., & Miesch, M. S. 2009, *ApJ*, **692**, 1421
- D'Silva, S., & Choudhuri, A. R. 1993, *A&A*, **272**, 621
- Fan, Y., & Fang, F. 2014, *ApJ*, **789**, 35
- Fan, Y., Fisher, G. H., & McClymont, A. N. 1994, *ApJ*, **436**, 907
- Featherstone, N. A., & Miesch, M. S. 2015, *ApJ*, **804**, 67
- Gilman, P. A., & Dikpati, M. 2000, *ApJ*, **528**, 552
- Hale, G. E., Ellerman, F., Nicholson, S. B., & Joy, A. H. 1919, *ApJ*, **49**, 153
- Hathaway, D. H., & Upton, L. A. 2016, *JGRA*, **121**, 10
- Hazra, G., Choudhuri, A. R., & Miesch, M. S. 2017, *ApJ*, **835**, 39
- Hazra, G., Karak, B. B., Banerjee, D., & Choudhuri, A. R. 2015, *SoPh*, **290**, 1851
- Hazra, G., Karak, B. B., & Choudhuri, A. R. 2014, *ApJ*, **782**, 93
- Hazra, S., & Nandy, D. 2016, *ApJ*, **832**, 9
- Hotta, H., Rempel, M., & Yokoyama, T. 2016, *Sci*, **351**, 1427
- Hotta, H., & Yokoyama, T. 2010, *ApJL*, **714**, L308
- Howard, R. F. 1991, *SoPh*, **136**, 251
- Işık, E. 2015, *ApJL*, **813**, L13
- Jackiewicz, J., Serebryanskiy, A., & Kholikov, S. 2015, *ApJ*, **805**, 133
- Jiang, J., Cameron, R. H., & Schüssler, M. 2014, *ApJ*, **791**, 5
- Jiang, J., Chatterjee, P., & Choudhuri, A. R. 2007, *MNRAS*, **381**, 1527
- Jouve, L., & Brun, A. 2007, *A&A*, **474**, 239
- Käpylä, M. J., Käpylä, P. J., Olsper, N., et al. 2016, *A&A*, **589**, A56
- Karak, B. B., & Brandenburg, A. 2016, *ApJ*, **816**, 28
- Karak, B. B., & Cameron, R. 2016, *ApJ*, **832**, 94
- Karak, B. B., & Choudhuri, A. R. 2011, *MNRAS*, **410**, 1503
- Karak, B. B., & Choudhuri, A. R. 2013, *RAA*, **13**, 1339
- Karak, B. B., Jiang, J., Miesch, M. S., Charbonneau, P., & Choudhuri, A. R. 2014a, *SSRv*, **186**, 561
- Karak, B. B., Käpylä, P. J., Käpylä, M. J., et al. 2015, *A&A*, **576**, A26
- Karak, B. B., & Nandy, D. 2012, *ApJL*, **761**, L13
- Karak, B. B., Rheinhardt, M., Brandenburg, A., Käpylä, P. J., & Käpylä, M. J. 2014b, *ApJ*, **795**, 16
- Kitchatinov, L. L., & Olemskoy, S. V. 2011, *AstL*, **37**, 656
- Kitchatinov, L. L., Pipin, V. V., & Ruediger, G. 1994, *AN*, **315**, 157
- Komm, R. W., Howard, R. F., & Harvey, J. W. 1995, *SoPh*, **158**, 213
- Leighton, R. B. 1964, *ApJ*, **140**, 1547
- Lemerle, A., & Charbonneau, P. 2017, *ApJ*, **834**, 133
- Lemerle, A., Charbonneau, P., & Carignan-Dugas, A. 2015, *ApJ*, **810**, 78
- Li, D. 2017, *RAA*, **17**, 40
- Lopes, I., & Passos, D. 2009, *SoPh*, **257**, 1
- McClintock, B. H., Norton, A. A., & Li, J. 2014, *ApJ*, **797**, 130
- McIntosh, S. W., Leamon, R. J., Gurman, J. B., et al. 2013, *ApJ*, **765**, 146
- McIntosh, S. W., Leamon, R. J., Krista, L. D., et al. 2015, *NatCo*, **6**, 6491
- Miesch, M. S., & Dikpati, M. 2014, *ApJL*, **785**, L8
- Miesch, M. S., Featherstone, N. A., Rempel, M., & Trampedach, R. 2012, *ApJ*, **757**, 128
- Miesch, M. S., & Teweldebirhan, K. 2016, *SSRv*, **58**, 1571
- Muñoz-Jaramillo, A., Dasi-Espuig, M., Balmaceda, L. A., & DeLuca, E. E. 2013, *ApJL*, **767**, L25
- Muñoz-Jaramillo, A., Senkpeil, R. R., Windmueller, J. C., et al. 2015, *ApJ*, **800**, 48
- Nordlund, Å., Stein, R. F., & Asplund, M. 2009, *LRSP*, **6**, 2
- Olemskoy, S. V., & Kitchatinov, L. L. 2013, *ApJ*, **777**, 71
- Parfrey, K. P., & Menou, K. 2007, *ApJL*, **667**, L207
- Parker, E. N. 1979, *Cosmical Magnetic Fields: Their Origin and Their Activity* (Cambridge: Cambridge Univ. Press)
- Passos, D., Nandy, D., Hazra, S., & Lopes, I. 2014, *A&A*, **563**, A18
- Priyal, M., Banerjee, D., Karak, B. B., et al. 2014, *ApJL*, **793**, L4
- Rajaguru, S. P., & Antia, H. M. 2015, *ApJ*, **813**, 114
- Schatten, K. H., Scherrer, P. H., Svalgaard, L., & Wilcox, J. M. 1978, *GeoRL*, **5**, 411
- Schrijver, C. J., & Harvey, K. L. 1994, *SoPh*, **150**, 1
- Senthamizh Pavai, V., Arlt, R., Dasi-Espuig, M., Krivova, N. A., & Solanki, S. K. 2015, *A&A*, **584**, A73
- Simard, C., Charbonneau, P., & Dube, C. 2016, *AdSpR*, **58**, 1522
- Solanki, S. K., Wenzler, T., & Schmitt, D. 2008, *A&A*, **483**, 623
- Spruit, H. 1997, *MmSAI*, **68**, 397
- Stenflo, J. O., & Kosovichev, A. G. 2012, *ApJ*, **745**, 129
- Upton, L., & Hathaway, D. H. 2014, *ApJ*, **792**, 142
- Usoskin, I. G. 2013, *LRSP*, **10**, 1
- Usoskin, I. G., Solanki, S. K., & Kovaltsov, G. A. 2007, *A&A*, **471**, 301
- Wang, Y.-M., Colaninno, R. C., Baranyi, T., & Li, J. 2015, *ApJ*, **798**, 50
- Wang, Y.-M., & Sheeley, N. R. 2009, *ApJL*, **694**, L11
- Wang, Y.-M., & Sheeley, N. R., Jr. 1989, *SoPh*, **124**, 81
- Yeates, A. R., Nandy, D., & Mackay, D. H. 2008, *ApJ*, **673**, 544
- Zhang, J., Wang, Y., & Liu, Y. 2010, *ApJ*, **723**, 1006
- Zhao, J., & Chen, R. 2016, *AsJPh*, **25**, 325